An Unusual Case of Rapid Cyclogenesis in the Northeast Pacific Basin. Overview and Piecewise PV Inversion

PATRICK T. BEATY,[a] JONATHAN E. MARTIN,[a] ANDREW C. WINTERS,[b] AND GARY M. LACKMANN[c]

[a] *University of Wisconsin–Madison, Madison, Wisconsin*
[b] *University of Colorado Boulder, Boulder, Colorado*
[c] *North Carolina State University, Raleigh, North Carolina*

(Manuscript received 2 October 2024, in final form 15 April 2025, accepted 30 April 2025)

ABSTRACT: A case of extremely rapid, record-setting extratropical cyclogenesis over the northeast Pacific Ocean in late November 2019 is examined. The development is of particular interest as much of the strengthening occurred in an unusual environment characterized by cold sea surface temperatures. Cyclogenesis began as a stationary upstream surface cyclone in the north-central Pacific ushered warm, moist tropical air poleward toward a preexisting surface frontal boundary, resulting in intense lower-tropospheric frontogenesis. The resulting thermally direct vertical circulation mobilized a diabatic Rossby wave (DRW) which moved eastward along the baroclinic zone. An intensifying upper-level jet/front system draping equatorward from Alaska became favorably aligned with the low-level DRW on its approach toward the California–Oregon border to force deepening rates as high as 6 hPa h^{-1} prior to landfall. The 3D Ertel potential vorticity (PV) structure associated with this storm is partitioned into separate upper-tropospheric, lower-tropospheric, and diabatically induced anomalies which are separately inverted to recover the flow associated with each piece. Analysis of this partitioned PV reveals that development followed a bottom-up sequence by which near-surface PV dominated early cyclogenesis, diabatically induced PV dominated a large period of subsequent intensification, and upper-tropospheric PV dominated the final period of development. Bottom-up developments of this intensity are rare. It is shown that diabatic influences in response to vigorous latent heat release are responsible for much of the lower-tropospheric cyclogenesis with an upper-level jet/front system becoming an important driver for the rapid cyclogenesis observed immediately before landfall.

SIGNIFICANCE STATEMENT: A rapidly developing low pressure system over the northeast Pacific Ocean in late November 2019 set all-time low pressure records and occurred in an unusual region of the world. The analysis shows that this development occurred from the bottom-up and midtropospheric latent heat release was the most important process leading to its record strength. It is very uncommon for low pressure systems of this intensity to follow a bottom-up development. More work is needed to determine how the upper- and lower-tropospheric features interacted with each other as they conspired to produce this record-setting low pressure system.

KEYWORDS: Cyclogenesis/cyclolysis; Potential vorticity; Diabatic heating; Synoptic-scale processes; Rossby waves; Inversions

1. Introduction

Rapid extratropical cyclogenesis, colloquially known as "bomb" cyclogenesis (e.g., Sanders and Gyakum 1980; Roebber 1984), arises from a variety of different dynamical and thermodynamical factors including the interaction between upper-tropospheric troughs and lower-tropospheric baroclinic zones (e.g., Sanders 1986; Gyakum et al. 1992; Lagouvardos et al. 2007; Heo et al. 2019), diabatic heating in the form of latent heat release (e.g., Bosart 1981; Roebber 1993; Martin and Otkin 2004; Terpstra et al. 2015; Kohl and O'Gorman 2022), and/or sea surface heat fluxes (e.g., Davis and Emanuel 1988; Roebber 1989; Kuo et al. 1991; Gyakum and Danielson 2000; Kouroutzoglou et al. 2015). In addition, the interaction between a diabatic Rossby wave (DRW) and an upper-tropospheric trough (e.g., Wernli et al. 2002; Moore et al. 2008; Rivière et al. 2010; Boettcher and Wernli 2011, 2013; McKenzie 2014; Tamarin and Kaspi 2016; Zhang and Wang 2018) is a particular kind of rapid cyclogenesis event. The concept of a DRW was introduced in a series of studies in the early 1990s (i.e., Raymond and Jiang 1990; Snyder and Lindzen 1991; Parker and Thorpe 1995). The latter two studies employed highly idealized models with cloud-diabatic feedbacks in the vicinity of lower-troposphere baroclinic zones to consider both the production and subsequent evolution of positive low-level potential vorticity (PV) anomalies beneath the location of maximum cloud production.

Studies by Moore and Montgomery (2004, 2005) were the first to classify such low-level PV anomalies as diabatically generated vortices. The interaction between the associated cyclonic flow around such a vortex and the baroclinic zone along which it forms acts to provide continued positive moisture and temperature advections downstream of the vortex. These advections contribute to the production of clouds and precipitation, which regenerate the lower-tropospheric cyclonic PV anomaly downstream, thereby appearing to propagate the original anomaly downstream (Terpstra et al. 2015; Tamarin and Kaspi 2016; Kohl and O'Gorman 2022).

In late December 1999, storm "Lothar" devastated portions of western Europe, becoming the costliest windstorm in

Corresponding author: Patrick T. Beaty, pbeaty@wisc.edu

DOI: 10.1175/MWR-D-24-0198.1

European history in terms of structural and ecological damage (Wernli et al. 2002). Focusing their analysis of the event on the evolution of Lothar as a DRW, Wernli et al. (2002) showed that Lothar underwent a "bottom-up" development in which the lower-tropospheric cyclonic PV anomaly (the DRW), acting on an initially zonal upper-tropospheric flow, induced upper-tropospheric trough development which eventually enabled a superposition of upper- and lower-tropospheric PV features. Though bottom-up development of explosive DRWs with no preexisting upper-tropospheric trough is rare (Boettcher and Wernli 2013), such a configuration served to initiate the mutual amplification of the two features which was manifested in the rapid development of Lothar. Rivière et al. (2010) employed the Météo-France operational model to perform a sensitivity analysis on the development of Lothar and, though the analysis was centered around the investigation of Lothar, the conclusions were extended to the explosive development of DRWs in general. They found that the explosive growth stage of rapidly developing DRWs such as Lothar is highly dependent on 1) moist processes to overcome frictional and turbulent dissipation, 2) the location of the upper-tropospheric jet exit region to aid in synoptic-scale ascent, and 3) a lower-tropospheric baroclinic zone to encourage DRW self-sustenance.

Boettcher and Wernli (2011) used four European Centre for Medium-Range Weather Forecasts (ECMWF) model forecasts initialized at different lead times along with a DRW-tracking algorithm to interrogate the influence of downstream lower-tropospheric temperature and moisture advections on rapid DRW developments. Boettcher and Wernli (2013) constructed a 10-yr climatology of DRWs in the Northern Hemisphere based on the tracking algorithm developed in Boettcher and Wernli (2011). These consecutive studies led to the identification of four precursor environments favorable for DRW genesis: 1) a broad subtropical high advecting warm air and moisture toward a baroclinic zone, 2) a cutoff low or remnant tropical cyclone advecting warm air and moisture toward a baroclinic zone, 3) an upper-tropospheric trough moving over a lower-tropospheric baroclinic zone, and 4) the remnants of a tropical cyclone or mesoscale convective system propagating along a baroclinic zone as a lower-tropospheric vortex. Frequent locations of rapid DRW developments in the Northern Hemisphere were along the Gulf Stream in the Atlantic Ocean and following the climatological North Pacific wintertime jet (Boettcher and Wernli 2013). In addition, they suggested that most cases of explosive DRW development involve a DRW interacting with a preexisting upper-tropospheric trough.

Moore et al. (2008) and Rivière et al. (2010) both took advantage of the utility of the piecewise PV inversion method introduced by Davis and Emanuel (1991) to attribute the intensification of a DRW cyclogenesis event to discrete pieces of the full column PV. The cases chosen for both studies were DRWs propagating over warm sea surface temperatures (SSTs) which provide substantial surface heat and moisture fluxes to aid in the rapid strengthening of the DRW (e.g., Davis and Emanuel 1988; Roebber 1989; Kuo et al. 1991; Gyakum and Danielson 2000; Kouroutzoglou et al. 2015). To the best of the authors' knowledge, a similar analysis on an explosive DRW development over a cold ocean surface (<12°C) has not yet been performed. DRW developments over such cold ocean surfaces represented an estimated 5% of *all* tracked DRWs in the Boettcher and Wernli (2013) climatology.

From 0000 UTC 26 November 2019 to 0000 UTC 27 November 2019, a DRW, originating at the intersection of a high θ_e tropical moisture plume and a zonally oriented baroclinic zone, underwent rapid cyclogenesis over the northeast Pacific Ocean. DRW intensification followed the description offered by Boettcher and Wernli (2013), wherein low-level diabatically generated PV associated with the DRW vortex became vertically collocated with an upper-tropospheric PV anomaly borne of a downward and equatorward surge of stratospheric air. Hourly fifth generation ECMWF atmospheric reanalysis (ERA5; Hersbach et al. 2020) data suggest that this superposition of forcings resulted in a remarkable mean sea level pressure (MSLP) fall of 49 hPa in 24 h as the DRW progressed east-southeastward toward the U.S. West Coast. As the storm neared landfall, the MSLP dropped 12 hPa between 1600 UTC 26 November and 1900 UTC 26 November, including a 1-h central MSLP fall of 6 hPa from 1700 UTC 26 November to 1800 UTC 26 November 2019. The observed MSLP minimum of 973.4 hPa at Crescent City, California, at 0300 UTC 27 November 2019 set the all-time low sea level pressure record for the state of California. November low sea level pressure records were also observed in Medford, Oregon (981.4 hPa), and Eureka, California (984.4 hPa), on the same date.

The November 2019 (hereafter NV19) cyclone provides an opportunity to interrogate the nature of an explosive DRW development over a cold ocean surface. The analysis will center on a piecewise PV inversion of this particular cyclone following the method of Davis and Emanuel (1991). Comparing this event to those previously examined (over warm SSTs) will highlight physical precursors critical for rapid DRW-induced development in such an otherwise unfavorable environment. The paper is organized as follows. An overview of the reanalysis data and the piecewise PV inversion method utilized in this study is detailed in section 2. Section 3 provides a synoptic evolution of the life cycle of the November 2019 cyclone from 12 h before genesis to postocclusion and affirms that this is a DRW-induced development while highlighting its exceptional nature. The evolution of the life cycle of the storm through the lens of piecewise PV inversion is discussed in section 4. Comparison of this event to the bottom-up development of Lothar along with conclusions and suggestions for further analysis is offered in section 5.

2. Data and methods

a. Dataset

Wind speed and direction, temperature, geopotential height, relative humidity, and MSLP data for the NV19 storm were extracted on a limited-area domain extending from 10° to 75°N and from 180° to 90°W from the ERA5 dataset. The analysis employs ERA5 data at 1-h intervals from 0000 UTC 1 November 2019 to 2300 UTC 31 December 2019 with a horizontal grid spacing

of 0.25° × 0.25° and 19 vertical levels from 1000 to 100 hPa at a vertical grid spacing of 50 hPa. ERA5 data were then regridded to a grid spacing of 1.0° × 1.0° as coarse data with smooth gradients are more amenable to the PV inversion process (Hoskins et al. 1985). ERA5 hourly MSLP and wind data were compared with the 3-hourly Weather Prediction Center and the 6-hourly Ocean Prediction Center Pacific surface observations to confirm their accuracy.

b. *Piecewise PV inversion*

First envisioned by Rossby (1940), Ertel (1942) expressed the potential vorticity [often referred to as the Ertel PV (EPV)] as

$$\mathrm{EPV} = -g\,(\zeta_\theta + f)\frac{\partial\theta}{\partial p}, \tag{1}$$

where g is gravitational acceleration, ζ_θ is the isentropic relative vorticity, f is the planetary vorticity, and $\partial\theta/\partial p$ is a static stability term. EPV is conserved for adiabatic, inviscid flow. Information about the atmospheric flow associated with a distribution of EPV can be extracted through the process of PV inversion (Hoskins et al. 1985; Davis and Emanuel 1991). The inversion of a distribution of PV, often done in pressure coordinates to avoid complexities of θ coordinates, requires knowledge of 1) a horizontal and vertical distribution of PV, 2) prescribed boundary conditions on the domain, and 3) a balance condition which relates the mass to the momentum field. It can be particularly enlightening to partition the PV field into discrete pieces each related to different vertical levels and/or physical processes involved in cyclogenesis, a technique known as *piecewise PV inversion* first introduced by Davis and Emanuel (1991, hereafter DE). Such a piecewise PV inversion isolates the mass and momentum fields associated with individual pieces of the total anomalous PV, thus enabling investigation of the effect of each piece on the overall circulation tendency and the advection of the other pieces of the PV. The way the PV is partitioned is thus crucially important to both the procurement and the precision of the resulting insights.

The DE inversion method assumes hydrostatic balance and that the magnitude of the rotational part of the flow is much larger than that of the divergent part of the flow. Applying these approximations to the divergence equation and (1) results in the system of equations, in spherical coordinates, used in the DE piecewise PV inversion:

$$\nabla^2\Phi = \nabla\cdot(f\nabla\psi) + \frac{2}{a^4\cos^2\phi}\frac{\partial\left(\frac{\partial\psi}{\partial\lambda},\frac{\partial\psi}{\partial\phi}\right)}{\partial(\lambda,\,\phi)}, \tag{2}$$

$$\mathrm{EPV} = \frac{g\kappa\pi}{p}\left[(f+\nabla^2\psi)\frac{\partial^2\Phi}{\partial^2\pi} - \frac{1}{a^2\cos^2\phi}\frac{\partial^2\psi}{\partial\lambda\partial\pi}\frac{\partial^2\Phi}{\partial\lambda\partial\pi} - \frac{1}{a^2}\frac{\partial^2\psi}{\partial\phi\partial\pi}\frac{\partial^2\Phi}{\partial\phi\partial\pi}\right], \tag{3}$$

where Φ is the geopotential, ψ is the nondivergent streamfunction, ϕ is the latitude, λ is the longitude, a is the radius of Earth, p is the pressure, $\kappa = R/c_p$, and π is the Exner function $[c_p(p/p_0)^\kappa]$, which serves as the vertical coordinate (DE). Equation (2), the nonlinear balance condition of Charney (1955), relates the wind and pressure fields according to the assumption that the rotational part of the flow is much larger than the divergent part of the flow, which has been shown to be a good approximation to observed atmospheric flows, especially for flows of the synoptic scale (e.g., Davis et al. 1996). The unbalanced portion of the flow corresponds primarily to the nondivergent component of the ageostrophic wind and cannot be recovered using PV inversion techniques (Davis et al. 1996). The nondivergent flow field recovered from piecewise PV inversion was compared to the pure ERA5 flow field across a 10° × 10° box centered on the NV19 MSLP minimum. Differences between these two flow fields did not exceed 20% for 950 hPa, 10% for 900 hPa, and 5% at and above 850 hPa meaning that piecewise PV inversion is accurately representing this development throughout the troposphere. These larger differences near the surface are directly attributed to stronger nondivergent ageostrophic components of the wind in the vicinity of the intense NV19 cyclone.

Piecewise PV inversion is accomplished by first performing an inversion on the full perturbation PV which is defined by subtracting the 2-month mean PV from the instantaneous PV at 1-h increments at each grid point during the development of the NV19 storm. For the full perturbation PV inversion, (2) and (3) are solved simultaneously for the hourly Φ and ψ, with the lateral boundary conditions for Φ and ψ prescribed by subtracting the 2-month mean Φ and ψ from the instantaneous ERA5 data. The boundary ψ was initialized using Neumann boundary conditions such that the component of the total wind from the ERA5 data which was perpendicular to the boundary was equivalent to the gradient of ψ along that same boundary and that the net divergence out of the domain was zero. Neumann boundary conditions consistent with hydrostatic balance were prescribed along the bottom (top) of the domain such that the vertically averaged perturbation potential temperature, defined following the same method used in calculating the perturbation PV, between 1000 and 950 hPa (150 and 100 hPa) was used to define Φ and ψ along the bottom (top) of the domain. Full static PV inversion was performed across the entire horizontal and vertical domain and, to assure a stable solution of (2) and (3), negative PV values were manually adjusted to a small positive constant of 0.01 PVU (where 1 PVU = 10^{-6} K kg^{-1} m^2 s^{-1}) and the static stability was required to remain positive throughout the domain. The threshold for convergence was set to 0.1 m, the overrelaxation parameters for Φ and ψ were 1.8 and 1.9, respectively, and the underrelaxation parameter was set to 0.3. Each hourly time step reached convergence after approximately 150 iterations. The reader is referred to DE for a complete description of the boundary conditions and numerical methods used to solve this system.

c. *Partitioning method*

The next step in performing piecewise PV inversion is to partition the full perturbation PV field into three distinct pieces. Here, we follow a modified version of the piecewise

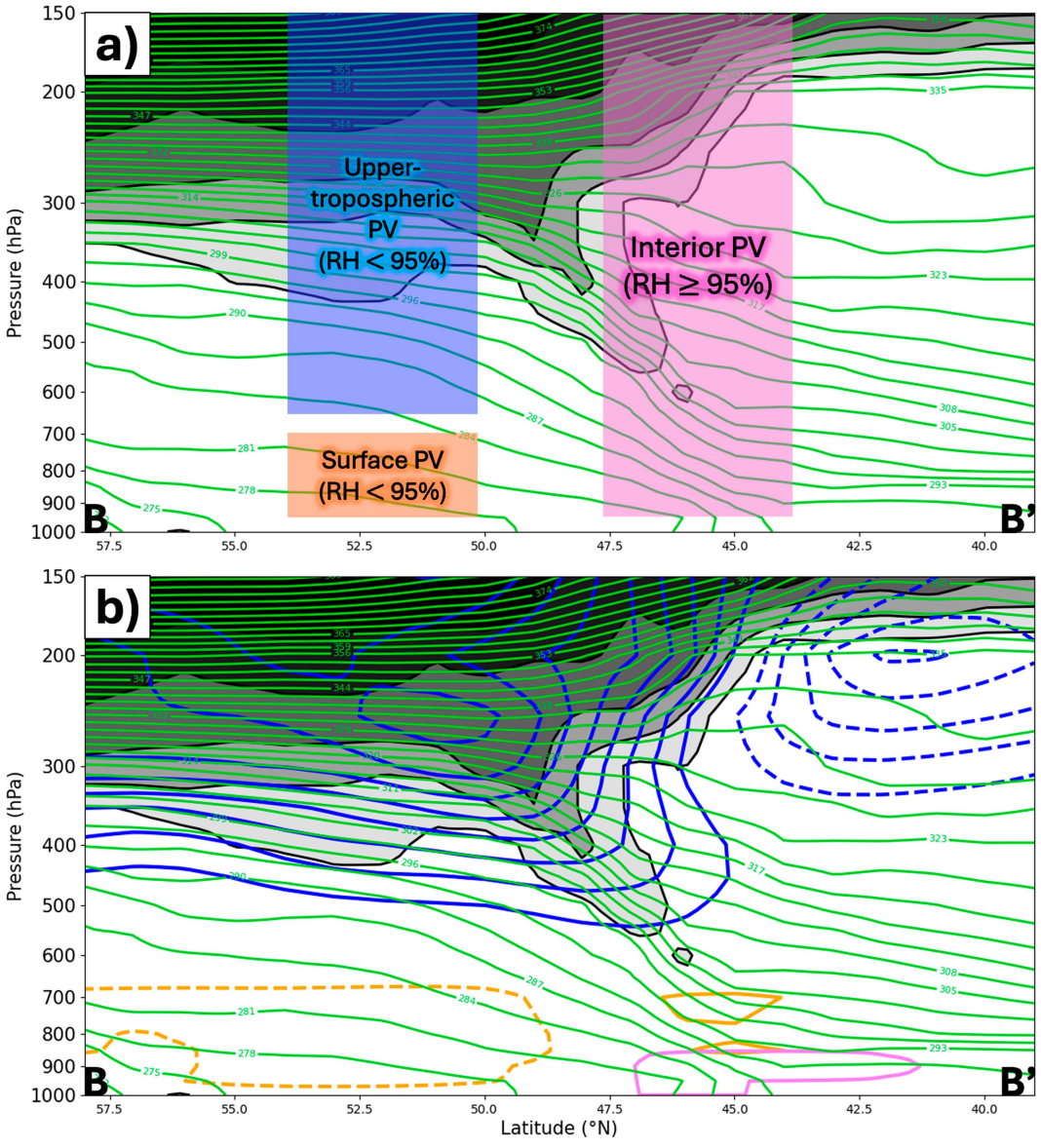

FIG. 1. Schematic of the piecewise partitioning scheme used in the inversion of the perturbation PV overlaid on a cross section along B–B′ in Fig. 4e. Solid, green contours are potential temperature contoured every 3 K starting at 300 K. PV is shaded in gray every 2 PVU starting at 2 PVU. Labeled boxes correspond to the three distinct pieces of the total perturbation PV with the top and bottom boundaries of each box indicating the isobaric layers included within those pieces. The criterion for relative humidity used to distinguish the pieces of PV is as indicated. (b) As in (a), but with the distribution of UPTROP perturbation PV (blue contours), INT perturbation PV (pink contours), and SFC perturbation PV (orange contours) at 1200 UTC 26 Nov 2019 contoured every 0.5 PVU. Positive (negative) perturbation PV anomalies are denoted by the solid (dashed) contours.

partitioning described in Davis (1992), Korner and Martin (2000), and Winters and Martin (2017) which employs both isobaric and relative humidity criteria. Both the partitioning and the consequent analysis were found to be insensitive to a robust, but physically reasonable range of choices considered for the RH threshold (not shown).

The three-way partitioning method used in this study is depicted in Fig. 1. The surface (SFC) PV is defined as perturbation PV between 950 and 700 hPa in air with a relative humidity $<$ 95% and also includes the perturbation potential temperature on the bottom boundary of the domain. SFC is designed to represent the influence of near-surface potential temperature perturbations on the flow throughout the domain, as these are equivalent to PV perturbations along the bottom boundary (Bretherton 1966). The interior (INT) PV is defined as the perturbation PV between 950 and 150 hPa found in air with a relative humidity $\geq$ 95%. INT is

designed to represent the influence of diabatic generation and erosion of PV associated with latent heat release, a process central to DRW propagation (Boettcher and Wernli 2013; Terpstra et al. 2015; Tamarin and Kaspi 2016; Kohl and O'Gorman 2022). Therefore, INT can be considered a residual representing both the influence of diabatic processes and other remnant PV anomalies. The upper-tropospheric (UPTROP) PV is defined as the perturbation PV between 650 and 150 hPa found in air with a relative humidity $< 95\%$ and includes the perturbation potential temperature on the top boundary of the domain. UPTROP is designed to isolate the role of dry middle- and upper-tropospheric and stratospheric PV intrusions on the flow, along with stratospheric potential temperature anomalies.

Static inversion is performed for the SFC and UPTROP PV as for the full perturbation PV, but with Φ and ψ on the horizontal boundaries being set to zero. Inversion of the INT PV is not performed; rather, its associated Φ and ψ ($\Phi_{\rm INT}$ and $\psi_{\rm INT}$, respectively) are presented as

$$\Phi_{\rm INT} = \Phi_{\rm FULLPERT} - (\Phi_{\rm SFC} + \Phi_{\rm UPTROP}) \quad (4) \text{ and}$$

$$\psi_{\rm INT} = \psi_{\rm FULLPERT} - (\psi_{\rm SFC} + \psi_{\rm UPTROP}), \quad (5)$$

where $\Phi_{\rm INT}$ and $\psi_{\rm INT}$ on the horizontal boundaries are set equal to the full perturbation Φ and ψ, not zero. The decision to prescribe these results was motivated by numerous unsuccessful trials in which the static inversion of the INT PV, though reaching convergence, consistently returned unphysical results. Similar unphysical results are detailed in both Ahmadi-Givi et al. (2004) and Bracegirdle and Gray (2009). Those studies concluded that such results derive from a breakdown of the Charney nonlinear balance condition (Charney 1955) in regions where strong divergence becomes collocated with regions of strong diabatic heating. The development of the NV19 DRW was strongly influenced by diabatic heating collocated with the lower-tropospheric vortex; hence, the governing physics were well outside the requisite nonlinear balance in (2). In such situations, convergence to a solution for the INT PV, characterized by heavy diabatic modification for extended periods of time, will produce a result in which the wind field is not dynamically consistent with the pressure field and the DE system of equations for piecewise PV inversion will no longer be valid. As the present analysis seeks to isolate the influence of the INT PV on aspects of the development, calculating it as a residual affords a tenable means to that end given the circumstances. This residual also predominantly corresponds to moist diabatic processes, as the influences of radiation and turbulence on the PV are much smaller in magnitude on the timescales considered.

3. Synoptic evolution and anomalous nature

a. Overview

We use hourly data from the ERA5 (Hersbach et al. 2020) to describe the synoptic overview of the NV19 storm and will focus on 12-h increments from 1200 UTC 25 November 2019, prior to the nascent stage of development, to 0000 UTC 27 November 2019, past the period of its most rapid development and as the storm made landfall on the West Coast of the United States.

1) 1200 UTC 25 NOVEMBER 2019

Twelve hours before the NV19 storm developed its own closed circulation at sea level, a predominantly zonally oriented surface baroclinic zone, indicated by a strong gradient of 950-hPa equivalent potential temperature (θ_e) contours, was draped southeastward from an almost cutoff low pressure system to the west through the center of a strong surface anticyclone to the east (Fig. 2a). Though there was no closed isobar evident at this time, there was a 950-hPa relative vorticity maximum (yellow-highlighted "X") at the intersection of this baroclinic zone with a more meridionally oriented cold frontal baroclinic zone (Figs. 2a,b). The same baroclinic zones were reflected in the isentropes at 850 hPa, with strong positive frontogenesis occurring due east of the 950-hPa vorticity maximum along the warm front (Fig. 2c). Positive 2D frontogenesis, calculated using

$$\Im_{\rm 2D} = \frac{1}{|\nabla\theta|}\left[\left(\frac{\partial\theta}{\partial x}\right)\left(-\frac{\partial \mathbf{V}}{\partial x}\cdot\nabla\theta\right) + \left(\frac{\partial\theta}{\partial y}\right)\left(-\frac{\partial \mathbf{V}}{\partial y}\cdot\nabla\theta\right)\right] \quad (6)$$

was maximized between 850 and 900 hPa along the baroclinic zone on which the cyclone developed, with negative omega (ascent) focused on the warm side of a deep baroclinic zone in response to that frontogenesis (Fig. 2d). At 500 hPa, the surface development region was downstream of the nearly cutoff low pressure center to the southwest and a shortwave feature to the northwest over the Alaska Peninsula (Fig. 2e). The surface development region was centered in the right entrance region of a downstream, anticyclonically curved jet streak at 300 hPa characterized by weak along-flow acceleration in the entrance region (Fig. 2f). A 300-hPa PV maximum over the Aleutians was the tropopause-level counterpart to the shortwave at 500 hPa (Figs. 2e,f).

2) 0000 UTC 26 NOVEMBER 2019

By 0000 UTC 26 November 2019, a weak surface cyclone was discernable along the baroclinic zone that stretched zonally through the anticyclone (Fig. 3a). This disturbance had begun to develop its own separate cloud feature by this time (Fig. 3b). The 850-hPa baroclinic zone and positive frontogenesis maintained its previous spatial relationship with the developing surface cyclone (Fig. 3c), with frontogenesis located to the east and northeast of the surface cyclone along the developing warm front. Positive frontogenesis was now maximized at 800 hPa as the frontal slope notably steepened from the previous time (cf. Figs. 2d–3d). In response to this evolution, the ascent associated with the lower-tropospheric frontogenesis was deeper. The shortwave feature at 500 hPa began to strengthen to the northwest of the surface cyclone, indicated by the increase in positive relative vorticity along the shortwave axis (Fig. 3e). The proximity of this shortwave resulted in a region of cyclonic vorticity advection (CVA) by the thermal wind, indicative of column mean divergence and

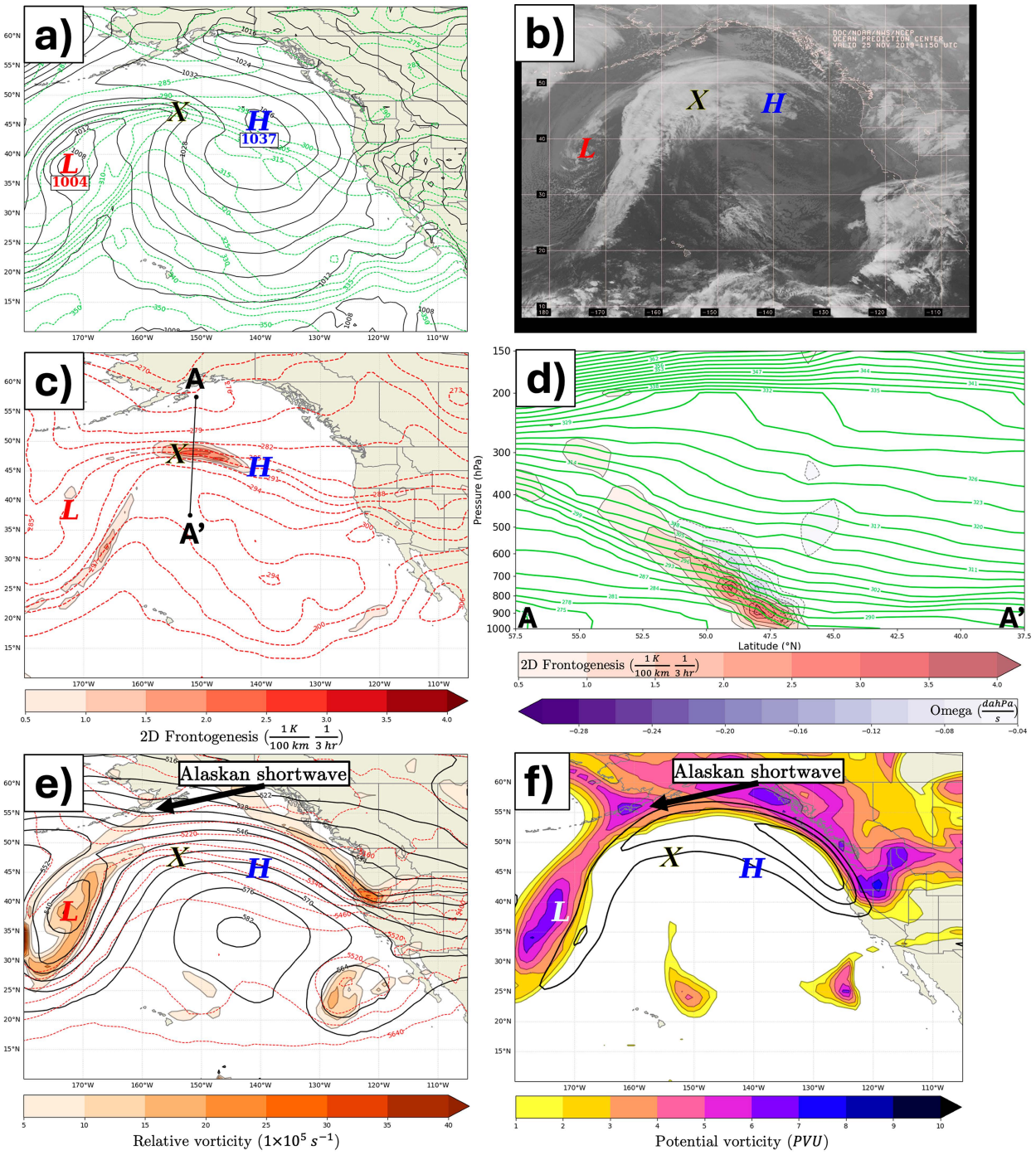

FIG. 2. (a) Sea level pressure and 950-hPa equivalent potential temperature (θ_e) from the ERA5 reanalysis valid at 1200 UTC 25 Nov 2019. Solid, black lines are isobars contoured every 4 hPa. Dashed, green lines are 950-hPa moist isentropes contoured every 5 K. "H" denotes the centers of high pressure systems whereas "L" denotes the centers of low pressure systems. "X" denotes the development region of the NV19 storm. (b) *GOES-17* infrared imagery of the northeast Pacific basin valid at 1150 UTC 25 Nov 2019. (c) Potential temperature and positive horizontal frontogenesis at 850 hPa from the ERA5 reanalysis valid at 1200 UTC 25 Nov 2019. Dashed, red contours are isentropes contoured every 3 K. Shading indicates positive frontogenesis function values shaded every 0.5 K (100 km)$^{-1}$ (3 h)$^{-1}$ starting at 0.5 K (100 km)$^{-1}$ (3 h)$^{-1}$. The black line indicates the cross section shown in (d). (d) Cross section along A–A′ in (c) of potential temperature, frontogenesis, and negative omega valid at 1200 UTC 25 Nov 2019. Potential temperature (green) contoured every 3 K starting at 300 K. Positive frontogenesis function (red shading) shaded every 0.5 K (100 km)$^{-1}$ (3 h)$^{-1}$. Negative omega (purple dashed shading) shaded every −0.04 daPa s^{-1} starting at −0.04 daPa s^{-1}. (e) The 1000–500-hPa thickness and relative vorticity at 500 hPa from the ERA5 reanalysis valid at 1200 UTC 25 Nov 2019. Red dashed contours are lines of constant thickness contoured every 60 m. Shading indicates positive

ascent (Sutcliffe 1947), coincident with the surface cyclone at this time. At 300 hPa, the surface cyclone maintained its position relative to the right entrance region of the downstream, anticyclonically curved jet streak with now stronger along-flow speed change characterizing the entrance region (Fig. 3f). The shortwave feature at 300 hPa had also strengthened as indicated by the expanding region of large 300-hPa positive PV to the north-northwest of the surface cyclone (Fig. 3f).

3) 1200 UTC 26 NOVEMBER 2019

Twelve hours after initial development (Fig. 4a), the NV19 storm completely bisected the anticyclone within which it initially developed (see Fig. 3a). Well-defined cold and warm fronts now characterized the cyclone, as shown by the 950-hPa θ_e, with pressure troughs associated with both fronts. At this time, the storm was beginning its 12-h period of most rapid deepening as it approached the California–Oregon border. The storm was also beginning to transition from a baroclinic leaf (Weldon 1979) to a more classic comma shape (Fig. 4b). The primary band of positive frontogenesis at 850 hPa remained robust and associated with the surface warm front while a band of weaker, positive frontogenesis developed along the cold front (Fig. 4c). The cyclone center was now clearly located at the apex of the 850-hPa thermal ridge. Positive frontogenesis peaked at 700 hPa as the warm front neared its maximum strength and the associated ascent expanded and intensified throughout the depth of the mid- to lower troposphere, now being maximized around 750 hPa (Fig. 4d). Rapid intensification and elongation of the 500-hPa positive vorticity feature occurred to the west-northwest of the surface cyclone, coincident with a sharp temperature gradient, indicative of the development of a potent upper-level jet/front system (Fig. 4e). This intensification focused vigorous CVA by the thermal wind directly above the surface cyclone and, consequently, the central pressure of the NV19 storm began to rapidly drop. The trough in the 1000–500-hPa thickness also lagged the geopotential height trough resulting in along-flow cold air advection coincident with the 500-hPa relative vorticity maximum (Fig. 4e). The thermal gradient directly west of the cyclone had intensified within this same 12-h interval. The region of increased baroclinicity was reflected in an increase in wind speed at 300 hPa, at the base of the shortwave feature (Fig. 4f). This wind speed intensification also situated the NV19 storm in the left exit region of a newly formed jet streak tied to the development of the upper-level jet/front system (e.g., Shapiro 1981, 1983; Lackmann et al. 1997; Martin 2014), providing another mechanism for enhancing upper-tropospheric mass evacuation and lower-tropospheric cyclogenesis.

4) 0000 UTC 27 NOVEMBER 2019

In the 24 h after initial development, the storm had deepened a total of 47 hPa to a central MSLP of 971 hPa, well exceeding the definition of explosive cyclogenesis first defined in Sanders and Gyakum (1980) (Fig. 5a). In fact, the storm had deepened from 1020 hPa at 2200 UTC 25 November to 971 hPa at 2200 UTC 26 November, resulting in a maximum 24-h deepening rate of 49 hPa. At 0000 UTC 27 November, the NV19 storm was just a few hours from making landfall on the West Coast of the United States near Crescent City, California (Figs. 5a,b). The intense pressure gradient to the south of the cyclone center resulted in surface winds greater than 45 m s^{-1} near the California–Oregon border and 24-m waves off the California coast (094 Cape Mendocino buoy). By this time, the positive frontogenesis at 850 hPa associated with the warm front was undoubtedly influenced by the steep topography adjacent to the U. S. West Coast (Figs. 5c,d) as the frontal structure had clearly weakened (Fig. 5d). Lower-tropospheric ascent at this time reached its largest values of the cyclone life cycle, also undoubtedly influenced by the steep topography. A well-developed trough with substantial CVA by the thermal wind and an elongated streamer of vorticity at 500 hPa were both still forcing ascent in and around the surface cyclone (Fig. 5e), with the strongest CVA by the thermal wind situated south of the cyclone (not shown). The intensified vortex strip was a manifestation of the continued development of the associated upper-level jet/front system (Fig. 5e). The jet streak to the west of the surface cyclone increased in intensity and the surface cyclone remained in the left exit region as the jet raced southeastward on the upstream side of a newly carved out upper trough (Fig. 5f). The surface cyclone was now vertically stacked as the 300-hPa PV and 500-hPa vorticity were all maximized at the same location directly above the surface cyclone (Figs. 5e,f).

b. *The NV19 cyclone as a diabatic Rossby wave*

As first introduced by Raymond and Jiang (1990), Snyder and Lindzen (1991), and Parker and Thorpe (1995) and first classified by Moore and Montgomery (2004, 2005), a DRW is a lower-tropospheric vortex borne of positive PV production in the vicinity of a lower-tropospheric baroclinic zone that is situated below midtropospheric latent heat release. During the early development phase of the NV19 storm, a nearly cutoff low pressure system south of the Aleutian Islands and an expansive high pressure system off the coast of the Pacific Northwest conspired to produce a southerly flow which overan a predominantly zonal baroclinic zone stretching across the northeast Pacific Ocean at 1200 UTC 25 November 2019 (Fig. 6a). This flow induced strong lower-tropospheric frontogenesis which, in turn, spawned the production of precipitation along the baroclinic zone as indicated by the 12-h rainfall rates from the ERA5 data. The ERA5 12-h rainfall rates agreed with 24-h rainfall rates from the Integrated Multi-satellitE Retrievals for the Global Precipitation Measurement (GPM) mission (IMERG) in terms of spatial

←
relative vorticity shaded every 5×10^{-5} s^{-1} starting at 5×10^{-5} s^{-1}. (f) PV and wind speed at 300 hPa from the ERA5 reanalysis valid at 1200 UTC 25 Nov 2019. Solid, black contours are wind speeds contoured every 10 m s^{-1} starting at 50 m s^{-1}. Shading indicates PV at 300 hPa shaded every 1 PVU starting at 1 PVU. L denotes the low pressure system changed to light blue for visibility.

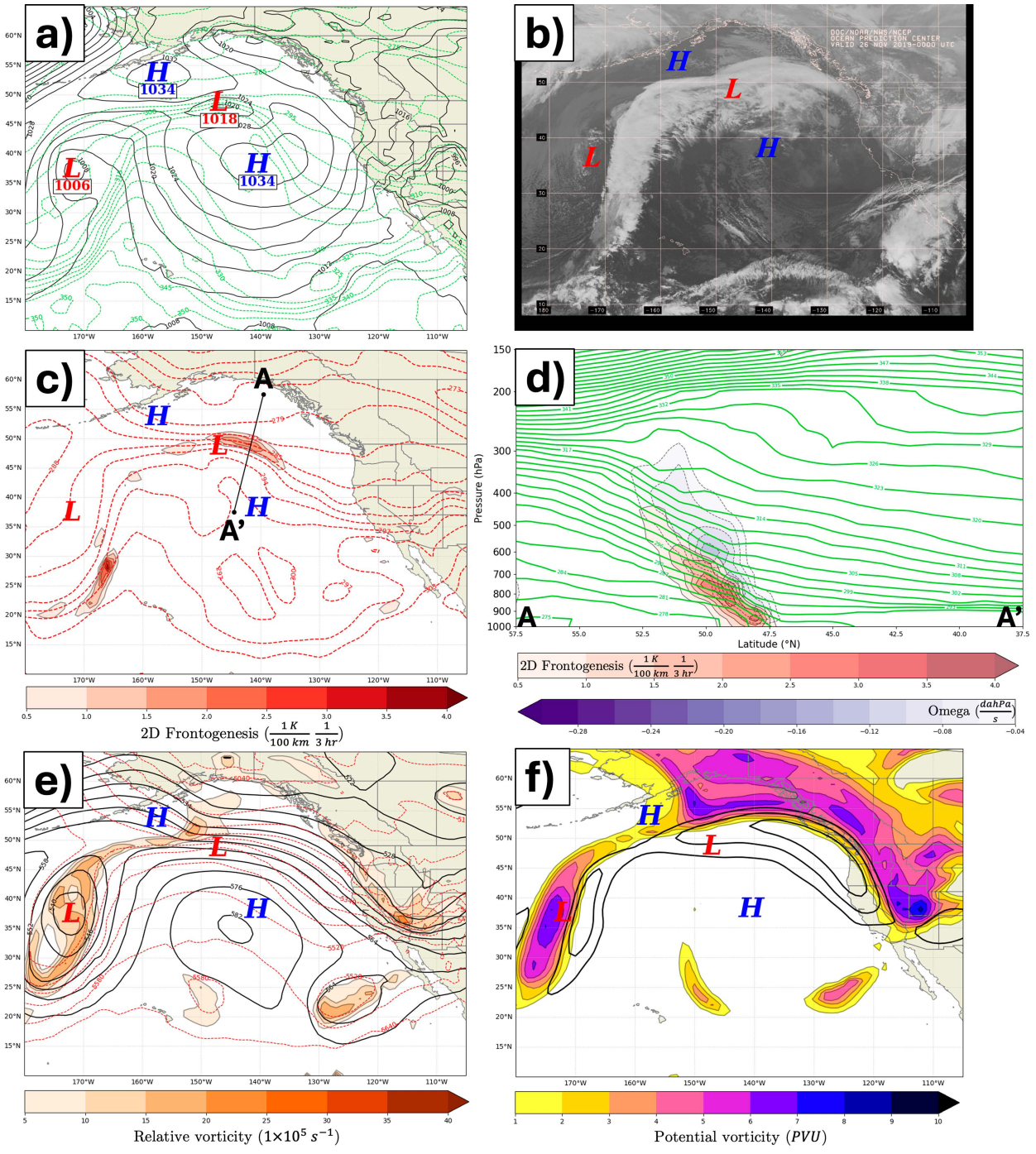

FIG. 3. (a) As in Fig. 2a, but for 0000 UTC 26 Nov 2019. (b) As in Fig. 2b, but for 0000 UTC 26 Nov 2019. (c) As in Fig. 2c, but for 0000 UTC 26 Nov 2019. (d) As in Fig. 2d, but for 0000 UTC 26 Nov 2019. (e) As in Fig. 2e, but for 0000 UTC 26 Nov 2019. (f) As in Fig. 2f, but for 0000 UTC 26 Nov 2019.

distribution and location of maxima (not shown). A lower-tropospheric circulation developed as a result of the latent heat release that accompanied the production of precipitation. This circulation then propagated along the baroclinic zone for at least the next 12 h as shown by the location of the SLP minimum along the mean 950-hPa θ_e gradient averaged between 1200 UTC 25 November 2019 and 0000 UTC 26 November 2019 (Fig. 6b). Thus, there was strong frontogenesis and moist ascent along the baroclinic zone (Figs. 2c,d and 3c,d) driving precipitation development and latent heat release which, in turn, mobilized lower-tropospheric diabatic PV "production" (Figs. 6a,b). The resulting diabatically generated vortex

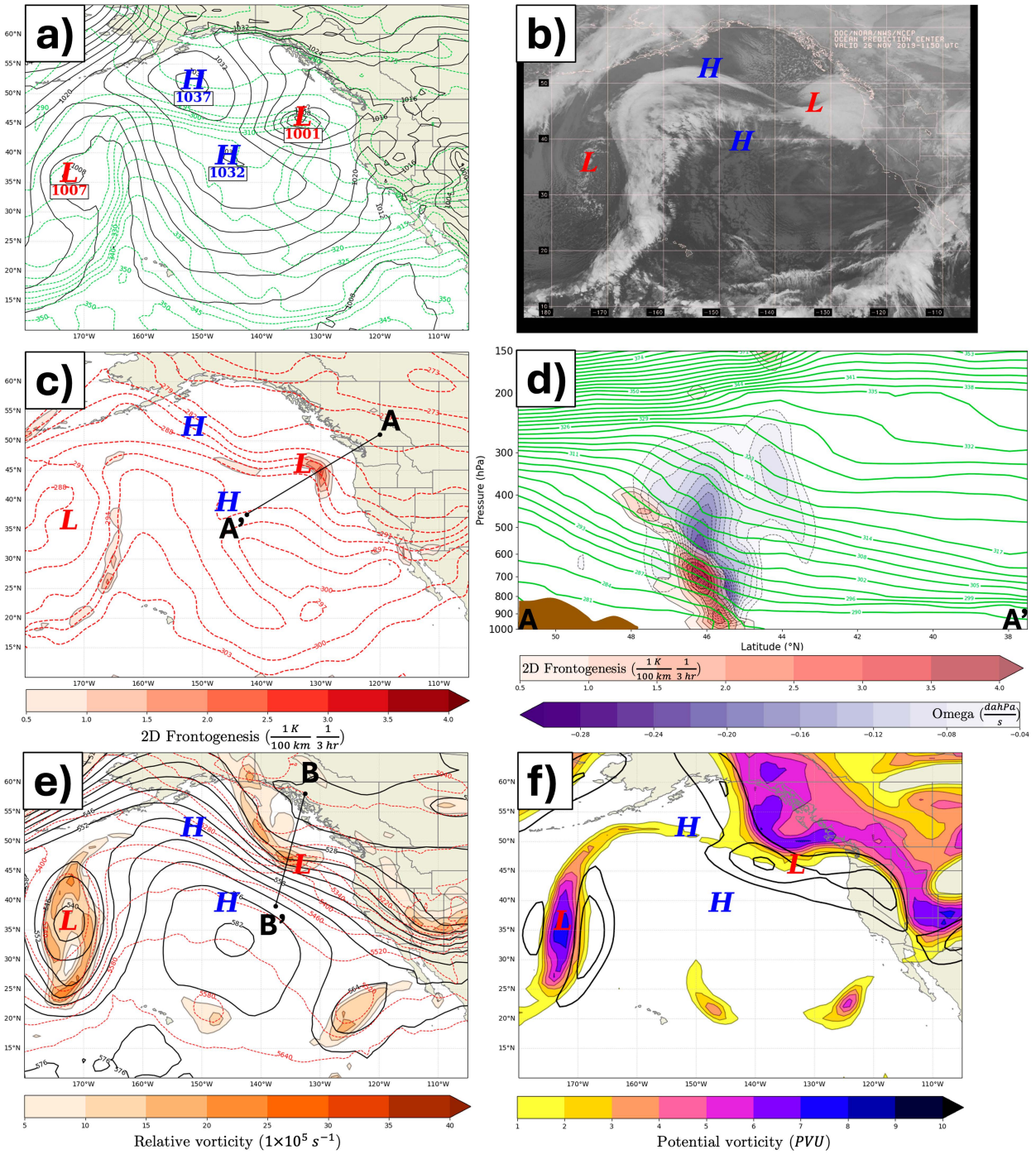

FIG. 4. (a) As in Fig. 3a, but for 1200 UTC 26 Nov 2019. (b) As in Fig. 3b, but for 1150 UTC 26 Nov 2019. (c) As in Fig. 3c, but for 1200 UTC 26 Nov 2019. (d) As in Fig. 3d, but for 1200 UTC 26 Nov 2019. (e) As in Fig. 3e, but for 1200 UTC 26 Nov 2019. (f) As in Fig. 3f, but for 1200 UTC 26 Nov 2019.

provided differential temperature advection near the surface which then propagated the DRW vortex. Propagation speeds averaged 24.4 m s^{-1} throughout the entire DRW life cycle with a maximum 1-hourly propagation speed of 47.6 m s^{-1} between 1200 UTC 26 November and 1300 UTC 26 November. This average far exceeded the threshold of 11.6 m s^{-1} for DRW propagation established in Boettcher and Wernli (2013) and neared the rapid average propagation speeds of ~30 m s^{-1} associated with Lothar (Wernli et al. 2002).

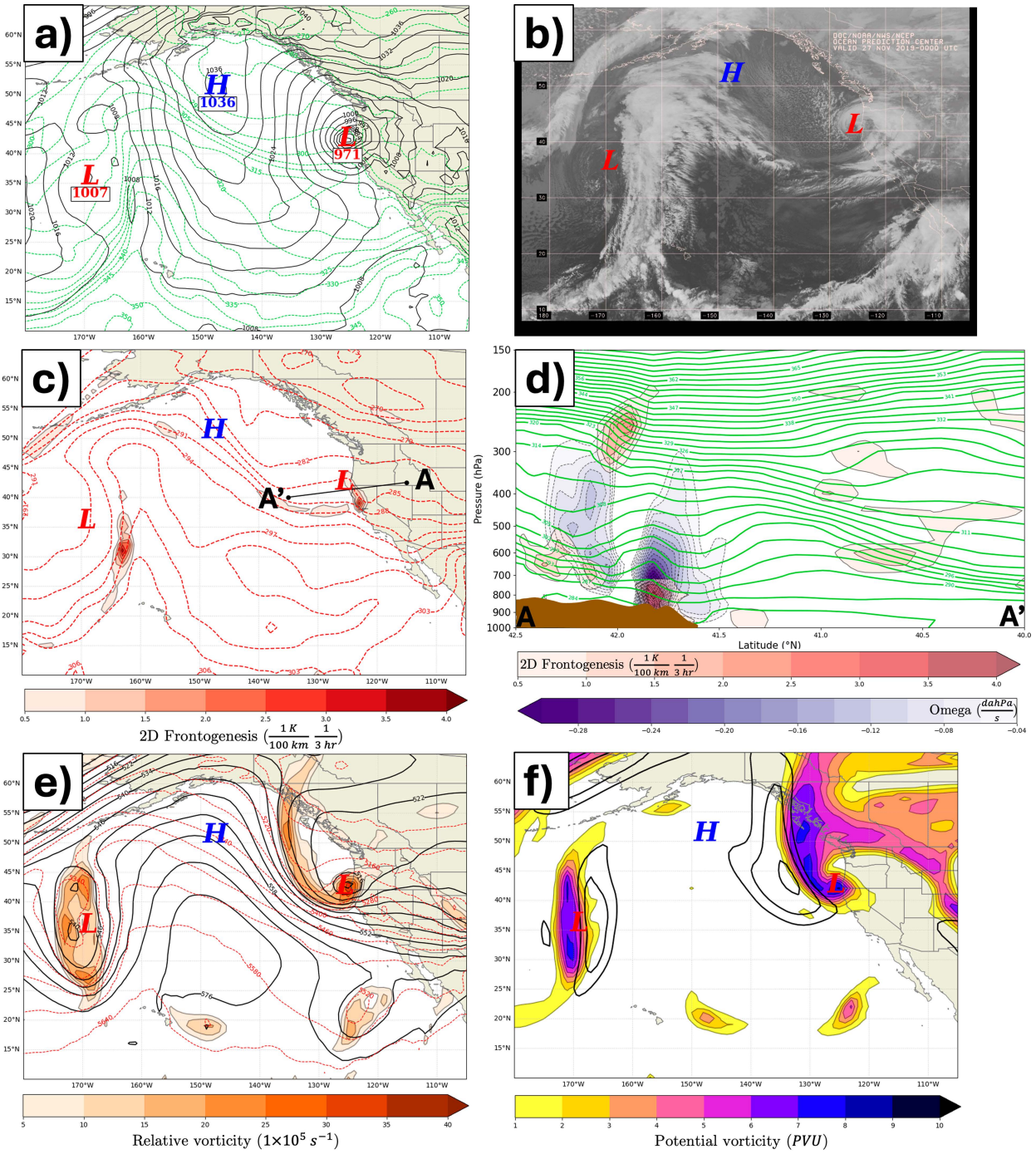

FIG. 5. (a) As in Fig. 4a, but for 0000 UTC 27 Nov 2019. (b) As in Fig. 4b, but for 0000 UTC 27 Nov 2019. (c) As in Fig. 4c, but for 0000 UTC 27 Nov 2019. (d) As in Fig. 4d, but for 0000 UTC 27 Nov 2019. (e) As in Fig. 4e, but for 0000 UTC 27 Nov 2019. (f) As in Fig. 4f, but for 0000 UTC 27 Nov 2019.

Last, the diabatic PV generation rate was assessed according to Eq. (74a) in Hoskins et al. (1985):

$$\dot{Q}_{\text{diab}} = Q\frac{\partial\dot{\theta}}{\partial p}\left(\frac{\partial\theta}{\partial p}\right)^{-1} - \dot{\theta}\frac{\partial Q}{\partial p}\left(\frac{\partial\theta}{\partial p}\right)^{-1}, \qquad (7)$$

where Q is the potential vorticity, θ is the potential temperature, and $\dot{\theta}$ is the potential temperature tendency, $\partial\theta/\partial t$. The generalized PV generation rate, which combines the effects of diabatic PV generation [first term on the right-hand side of (7)] and diabatic vertical advection of PV [second term on the

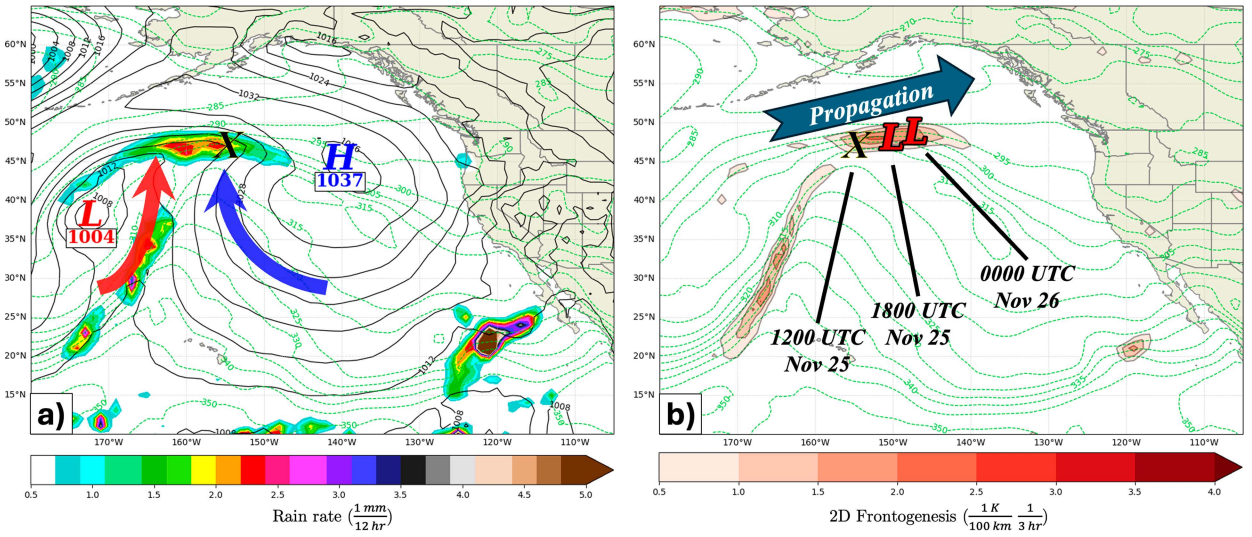

FIG. 6. (a) Sea level pressure and 950-hPa equivalent potential temperature θ_e from the ERA5 reanalysis valid at 1200 UTC 25 Nov 2019. Solid, black lines are isobars contoured every 4 hPa. Dashed, green lines are 950-hPa moist isentropes contoured every 5 K. Shading indicates the rainfall rate valid at 1800 UTC 25 Nov 2019 shaded every 0.25 mm 12 h^{-1} starting at 0.5 mm 12 h^{-1}. H denotes the center of the high pressure system whereas L denotes the centers of the low pressure systems. X denotes the development region of the NV19 storm. Red and blue annotated arrows indicate the lower-tropospheric synoptic-scale flow. (b) Propagation of sea level pressure minima along the 12-h mean 950-hPa θ_e between 1200 UTC 25 Nov 2019 and 0000 UTC 26 Nov 2019, as indicated by the arrow. Shading indicates the 12-h mean 950-hPa positive horizontal frontogenesis between 1200 UTC 25 Nov 2019 and 0000 UTC 26 Nov 2019 shaded every 0.5 K $(100\ km)^{-1}$ $(3\ h)^{-1}$. Moist isentropes contoured as in (a). L and X as in (a).

right-hand side of (7)], was averaged over two layers of near equal height following Kohl and O'Gorman (2022) and across a 10° × 10° box centered on the NV19 MSLP minimum throughout its evolution. The average rate of diabatic PV generation in the lower layer (LL), 950–550 hPa [upper layer (UL), 500–150 hPa], was zero (negative) as the DRW formed from 1800 UTC 25 November to 0000 UTC 26 November and then positive (remained negative) as the NV19 DRW strengthened and propagated eastward from 0000 UTC 26 November to 0900 UTC 26 November (Fig. 7). The positive PV anomaly in the lower layer, the NV19 DRW, and the negative PV anomaly in the upper layer were both growing through the diabatic generation of PV as DRW propagation and strengthening began, which agrees with the DRW growth mode presented in

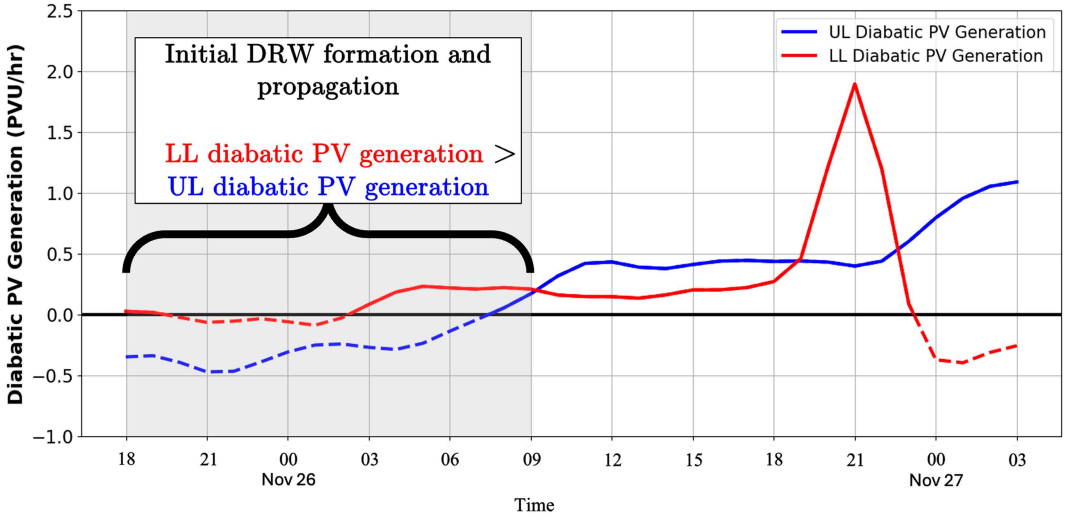

FIG. 7. The layer-averaged diabatic PV generation rate (PVU h^{-1}) for the upper layer (500–150 hPa; UL) and the lower layer (950–550 hPa; LL) from 1800 UTC 25 Nov 2019 to 0300 UTC 27 Nov 2019 averaged across a 10° × 10° box centered on the NV19 storm. Diabatic PV generation rate is contoured in solid blue for the UL and solid red for the LL with negative diabatic PV generation rates for both layers represented as dashed contours.

Kohl and O'Gorman (2022) and adds additional support to the notion that the NV19 storm originated as a DRW.

c. *The anomalous nature of the NV19 storm*

Northwesterly flow cyclogenesis events over the northeast Pacific Ocean are common and well documented (e.g., Reed and Albright 1986; Yoshiike and Kawamura 2009; Lang and Martin 2012; Iwao et al. 2012; Iizuka et al. 2013) along with explosive cyclogenesis (EC) events over this part of the Pacific Ocean (e.g., Roebber 1984; Wang and Rogers 2001; Boettcher and Wernli 2013; Zhang et al. 2017). Despite the relative frequency of EC events over the northeastern Pacific Ocean, the storm track, deepening rate, and location of maximum deepening for the NV19 storm were all well outside of established climatologies for this part of the world.

First, the NV19 storm had an unusual track. Roebber (1984) constructed a climatology of Northern Hemisphere EC events over the period from 1976 to 1982 while Wang and Rogers (2001) compiled a similar climatology for the period from 1985 to 1996. In still another climatology (from 2000 to 2015), Zhang et al. (2017) specifically focused on EC events over the northern Pacific Ocean. All three studies highlighted preferred regions for periodic EC events: off the east coast of Japan, off the East Coast of the United States, and in the central Gulf of Alaska. After genesis, a majority of the cyclones track southwest to northeast based on the roughly 30-yr period covered by the three, nonconsecutive climatologies. Tamarin and Kaspi (2016) noted that the predominant region of latent heat release associated with DRWs typically occurs to the northeast of the DRW center, which propagates the DRW eastward and poleward. The NV19 cyclone also initially formed in the central Gulf of Alaska and tracked nearly due east before beginning a northwest-to-southeast track (Figs. 2–5). Zhang et al. (2017) divided their database of EC storm tracks into separate regions of the northern Pacific in which clustering of cyclogenesis events occurred. The storm track of the NV19 cyclone was rotated approximately 90° to the right of both the northeastern Pacific Ocean EC storm tracks from the Zhang et al. (2017) climatology (their Fig. 5e) and the typical direction of DRW propagation from Tamarin and Kaspi (2016). The NV19 track was also mainly outside of the storm track densities presented in Roebber (1984), Wang and Rogers (2001), and Zhang et al. (2017). Thus, the storm track associated with the NV19 storm was unusual based on at least 30 years of nonconsecutive climatologies presented in the literature.

Second, the deepening rate of EC events has been quantified using the "Bergeron" since it was originally defined by Sanders and Gyakum (1980) as

$$1\ \text{Bergeron} = \frac{24\ \text{hPa}}{24\ \text{h}} \times \frac{\sin(\phi)}{\sin(60°)}, \tag{8}$$

where ϕ is the latitude of the cyclone center normalized to 60°N. A cyclogenesis event must accomplish a deepening rate equivalent to at least 1 Bergeron to be classified as explosive. Roebber (1984) and Zhang et al. (2017) used normalized latitudes of 42.5° and 45°, respectively, in the denominator of (8) as these mean latitudes were more representative of the mean latitude of explosive cyclogenesis events presented in their studies. The deepening rate of the NV19 storm using the Roebber (1984) and the Zhang et al. (2017) definitions was 2.14 Bergerons and 2.04 Bergerons, respectively. This deepening rate ranks the NV19 storm in the 99th percentile when focusing on the 115 EC cases over the northern Pacific Ocean from the Roebber (1984) climatology and in the 93rd percentile when focusing on the 120 EC cases over the northeast Pacific region from the Zhang et al. (2017) climatology. Further, the maximum 6-h deepening rate of 22 hPa between 1200 UTC 26 November 2019 and 1800 UTC 26 November 2019 rivals that of the maximum 6-h deepening rate of 26 hPa accomplished by the "Braer" storm, the strongest extratropical cyclone on record based on both minimum SLP and deepening rate (Lim and Simmonds 2002; Odell et al. 2013). Therefore, the maximum 6-h deepening rate of the NV19 storm was among the strongest ever recorded for all extratropical cyclones in the Pacific and Atlantic Ocean basins.

Finally, frequency contours of northern Pacific Ocean EC events are provided using the Roebber (1984), Wang and Rogers (2001), and Zhang et al. (2017) climatologies (Fig. 8). The furthest eastward extent of any of these frequency contours is 130°W (Fig. 8c). The maximum deepening of the NV19 storm occurred between 1700 UTC 26 November 2019 and 1800 UTC 26 November 2019 to the east of 130°W longitude. Out of a combined 30-yr period of northern Pacific Ocean EC events, no other EC event has had a maximum deepening location (MDL) as far east as the NV19 storm, yet another aspect of its anomalous nature.

4. Analysis

Subsequent analysis will concentrate on the 950-hPa isobaric surface as this level was the lowest available isobaric surface in the inversion output. Figure 9 compares 950-hPa geopotential height (Φ_{950}) at the location of the 950-hPa vorticity maximum of the NV19 storm from the ERA5 analyses and the full PV inversion. Though the full inversion results consistently return a higher Φ_{950}, the hourly positions demonstrate excellent agreement. The results of inverting the 2-month mean PV are not discussed as the analysis is primarily concerned with the perturbation PV introduced into the domain by the NV19 storm.

a. *Piecewise frontogenesis*

Piecewise PV inversion allows computation of the horizontal frontogenesis function [(6)] using the recovered balanced flow from the inversion of the full column perturbation PV and each of the three partitioned pieces of the perturbation PV. The goal is to determine which features in the perturbation PV distribution are controlling the strength and evolution of the initial lower-tropospheric frontogenesis (e.g., Korner and Martin 2000), as latent heat release within the thermally direct circulation, in response to the intense lower-tropospheric frontogenesis, spawned the DRW which became the NV19 storm (Figs. 2d, 3d, and 6). Therefore, we are only partitioning the balanced flow field, not the thermal field, and are considering the kinematic effects of the separate circulations on the total thermal field.

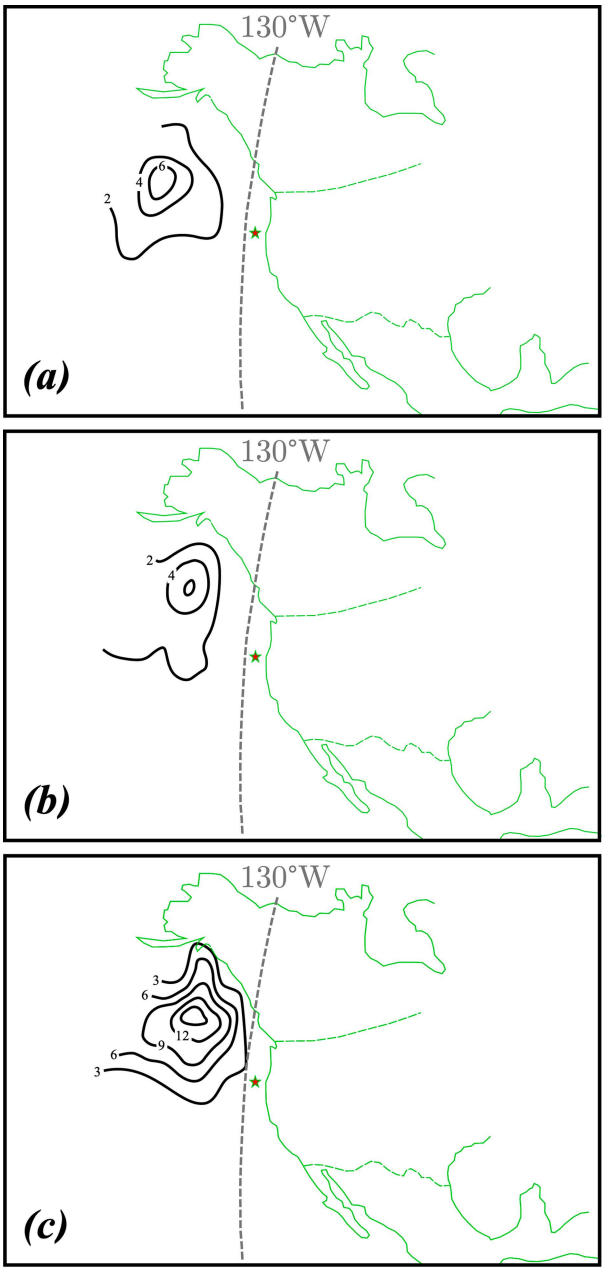

FIG. 8. Composite of maximum deepening locations (MDLs) for bomb cyclogenesis events over the northeastern Pacific Ocean as defined by Sanders and Gyakum (1980) and Zhang et al. (2017). (a) Adapted from Roebber (1984) for MDL between 1976 and 1982. The red star indicates MDL for the November 2019 storm. (b) Adapted from Wang and Rogers (2001) for MDL between 1985 and 1996. The red star indicates MDL for the November 2019 storm. (c) Adapted from Zhang et al. (2017) for MDL between 2000 and 2015. The red star indicates MDL for the November 2019 storm. The dashed, gray line indicates 130°W meridian.

1) 1200 UTC 25 NOVEMBER 2019

Ascent during the initial development of the NV19 storm was situated on the warm side of a frontogenesis maximum at 850 hPa forced by differential θ advection by the full perturbation (FULL PERT) balanced flow (Fig. 10a). There is good agreement between the distribution and orientation of the frontogenesis calculated using the FULL PERT balanced flow and the frontogenesis calculated using the ERA5 horizontal winds (cf. Figs. 2d and 10a). A majority of the FULL PERT frontogenesis was forced by the UPTROP PV balanced flow associated with the upstream upper-tropospheric shortwave (Figs. 2f and 10b). The balanced flow associated with the INT PV resulted in no notable frontogenesis along the cross section at this time (Fig. 10c). A strong, negative INT PV anomaly in the upper troposphere was located directly above the development region (not shown) due to persistent, differential lower-tropospheric high θ_e flow fueling convection along the baroclinic zone (e.g., Fig. 6a). Note that this negative upper-tropospheric INT PV anomaly is not the negative upper-*layer* PV anomaly referred to in Fig. 7 which propagates along with the DRW as a function of diabatic cooling (Kohl and O'Gorman 2022). Despite the emergence of a lower-tropospheric positive INT PV anomaly in response to the associated heating, the negative (upper tropospheric) piece of the INT PV exerted the predominant influence on the total INT PV-induced flow in the development region and, consequently, the INT PV contributed near-zero frontogenesis (Fig. 10c). The remaining portion of the lower-tropospheric frontogenesis was forced by the SFC PV balanced flow (Fig. 10d). This portion of perturbation frontogenesis was a result of anomalously warm near-surface potential temperatures underneath the 950- and 850-hPa thermal ridge stretching southwest of the development region which facilitated strong differential warm air advection in the lower troposphere across the baroclinic zone (Figs. 2a,c).

2) 0000 UTC 26 NOVEMBER 2019

The FULL PERT frontogenesis function became focused in the lower troposphere as the DRW vortex developed into a weak center of low pressure (Fig. 10e). There was still good agreement between the frontogenesis calculated using the FULL PERT balanced flow and the frontogenesis calculated using the ERA5 horizontal winds (cf. Figs. 3d and 10e). The perturbation frontogenesis forced by the UPTROP PV balanced flow was now both shallower and weaker as compared to 12 h prior (Figs. 10b,f). The DRW was still situated beneath an upper-tropospheric negative INT PV anomaly, and so the balanced flow from the INT PV once again resulted in insubstantial perturbation frontogenesis (Fig. 10g). At this time, the majority of the lower-tropospheric frontogenesis appeared forced by the balanced flow attributable to lower-tropospheric potential temperature perturbations (Figs. 3a,c and 10h). Perturbation southerly flow introduced via lower-tropospheric potential temperature anomalies provided most of the lower-tropospheric frontogenesis and subsequent latent heat release as NV19 DRW intensification and eastward propagation began.

b. Hourly height changes

After a coherent lower-tropospheric vortex had formed, the intensification of the NV19 storm was assessed by considering

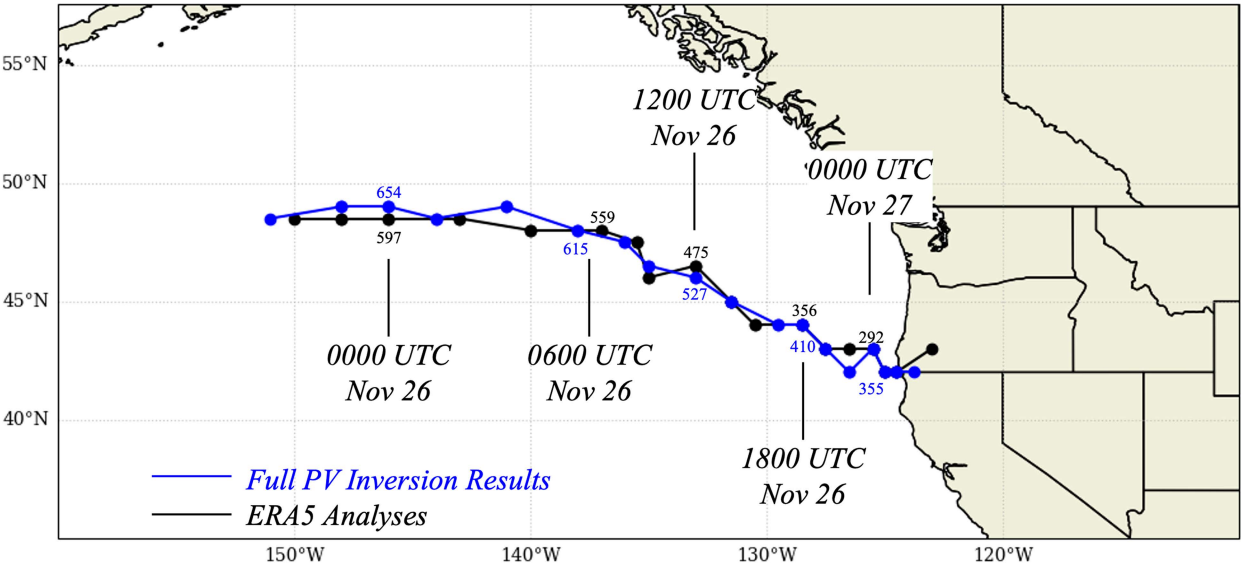

FIG. 9. Comparison of the full PV inversion results and the ERA5 analysis of storm track based on the location of the 950-hPa vorticity maxima. The location of vorticity maxima in the full PV inversion results is shown in blue with geopotential height at the vorticity maxima plotted in meters. The location of ERA5 analysis vorticity maxima is shown in black with geopotential height at the vorticity maxima plotted in meters.

the effects of each of the three pieces of the perturbation PV on near-surface height changes recovered from the piecewise PV inversion process. First, perturbation heights from the ERA5, FULL PERT, UPTROP, and SFC PV inversions, and the INT PV residual, were recorded at the location of the 950-hPa vorticity maximum associated with the NV19 storm. Then, the perturbation height change at time t, associated with the ERA5, full perturbation PV, and each of the three pieces, was the result of subtracting the perturbation heights at time $t + 1$ h from the perturbation heights at time $t - 1$ h and dividing by the time interval of 2 h. The results of these calculations are shown in Fig. 11, which displays the various height changes from 2100 UTC 25 November 2019 to 0600 UTC 27 November 2019.

Perturbation height changes from the ERA5 data and the inversion of the full perturbation PV were negative at the location of the 950-hPa vorticity maximum for a majority of the 33-h analysis period, with peak negative values occurring between 0900 UTC 26 November and 1300 UTC 26 November before exhibiting a steady increase until the end of the analysis period (Fig. 11a). The ERA5 and the full perturbation PV inversion height changes were in very good agreement. The 12-h maximum deepening period spanned from 0600 UTC 26 November to 1800 UTC 26 November, with the storm having experienced consecutive MSLP falls greater than 1 hPa h^{-1} beginning at 0900 UTC 26 November until making landfall. The influence of surface potential temperature anomalies on near-surface height changes was initially negative and then was negligible until the NV19 storm lost connection to surface baroclinicity after 1600 UTC 26 November (Fig. 11b). Diabatically induced PV had the most dominant influence throughout an overwhelming majority of the development (Fig. 11c). Near-surface height changes associated with the INT PV residual were negative beginning at 0000 UTC 26 November until the end of the storm life cycle, including throughout the entire 12-h maximum deepening period. In fact, INT PV contributed the most negative height changes during the early and late stages of cyclogenesis (Fig. 11). The influence of the UPTROP PV on near-surface height changes was minimal until 1500 UTC 26 November, by which time the developing upper-level jet/front system had finally encroached upon the NV19 storm, quickly inducing strong negative height changes (Fig. 11d). These height changes were the most negative of any associated with the three pieces of the perturbation PV directly outside of the 12-h maximum deepening period. Interrogations of the various physical mechanisms responsible for this period of development, including potential interaction between the lower-tropospheric DRW vortex and the upper-level jet/front system, which initially developed independently of each other, will be explored separately in future work.

c. *Mutual amplification*

The influence of specific PV anomalies (i.e., UPTROP, INT, and SFC) on the strength of the flow throughout the column is described via the PV superposition principle (DE; Morgan and Nielsen-Gammon 1998). The anomalous flow associated with, for instance, a UPTROP PV anomaly can interact with the INT PV distribution (at a given isobaric level) to amplify the magnitude of the INT PV anomaly via horizontal advection. In a statically stable atmosphere, local increases in EPV translate to increases in cyclonic circulation. Additionally, positive advection of lower boundary potential temperature anomalies by any discrete portion of the balanced flow will induce similar increases in cyclonic circulation (Bretherton 1966). Therefore, any location experiencing positive advection of perturbation EPV by a balanced flow, which would increase the anomalous

EPV there, will also experience an increase in the perturbation cyclonic circulation. Any such increase is a manifestation of the PV superposition principle and is labeled mutual cyclonic amplification.

The hour at which the associated perturbation height changes are most negative for the UPTROP, INT, and SFC PV (indicated by the starred times in Figs. 11b–d) is considered next. The analysis assesses if such favorable superposition among the various balanced flows attributable to the UPTROP, INT, and SFC PV contributed to an increase in the cyclonic flow throughout the column at these times during the NV19 storm.

1) 2100 UTC 25 NOVEMBER 2019

The initial near-surface height changes of the NV19 storm, from 2100 UTC 25 November to 2300 UTC 25 November, were predominantly driven by the influence of lower-boundary PV (Fig. 11b). The most negative of these 950-hPa height changes occurred at 2100 UTC 25 November, which corresponds to the time of initial formation of the SLP minimum which became the NV19 cyclone. Cyclonic PV advection (CPVA) by the balanced flow at three different isobaric levels from the inversion of the UPTROP and SFC PV and the INT PV residual at 2100 UTC 25 November is shown in Fig. 12. The yellow contours on each of the nine panels indicate where there is either appreciable CPVA or positive surface potential temperature advection by the balanced flow from a specified perturbation PV anomaly at the given isobaric level. In the upper troposphere, the balanced flows from the UPTROP and INT resulted in CPVA of upper-tropospheric PV to the north of the NV19 storm (Figs. 12a,b) while upper-tropospheric CPVA from the SFC balanced flow was occurring well to the northwest of the storm (Fig. 12c). No distinct diabatically induced PV anomaly had formed in the midtroposphere early in the storm life cycle, so no notable cyclonic advection of this type of PV was occurring (Figs. 12d–f). Cyclonic advection of lower-boundary PV by the UPTROP and INT balanced flows was not occurring in the vicinity of the NV19 storm (Figs. 12g,h). Only the balanced flow from the SFC was resulting in lower-boundary CPVA immediately over the NV19 storm center (Fig. 12i). Therefore, at this early time in storm development, lower-boundary CPVA was being amplified only by SFC anomalies, and no substantial mutual cyclonic amplification of PV anomalies throughout the depth of the troposphere was occurring.

2) 1400 UTC 26 NOVEMBER 2019

A majority of the subsequent cyclogenesis in terms of 950-hPa height changes was attributable to diabatically induced PV, which dominated near-surface intensification from 0000 UTC 26 November to 1600 UTC 26 November (Fig. 11c). Near-surface 1-hourly height changes associated with the diabatically induced PV were most negative at 1400 UTC 26 November, which was during the last hours of the 12-h period of most rapid deepening. At that time, the balanced flows from the inversion of the UPTROP and INT residual were responsible for CPVA of upper-tropospheric PV directly over the NV19 storm (Figs. 13a,b) while the balanced flow from the inversion of SFC induced CPVA well to the northwest (Fig. 13c). By this time, diabatic heating had generated a notable cyclonic midtropospheric PV anomaly due east of the surface cyclone. CPVA by the UPTROP and INT balanced flows was occurring to the east-southeast of the storm center (Figs. 13d,e). Advection of this midtropospheric PV by the balanced SFC winds was also occurring directly northeast of the storm (Fig. 13f). No appreciable advection of lower-boundary potential temperature by the UPTROP winds was occurring at this time (Fig. 13g). The balanced flow attributable to the INT resulted in lower-boundary CPVA to the southeast of the NV19 storm (Fig. 13h) while the SFC winds resulted in lower-boundary CPVA directly over the NV19 storm (Fig. 13i). Mutual cyclonic amplification throughout the column was ongoing at this time as CPVA induced by both UPTROP and INT was occurring in the upper troposphere (Figs. 13a,b), CPVA induced by UPTROP, INT, and SFC was evident in the midtroposphere (Figs. 13d–f), and CPVA induced by INT and SFC was ongoing in the lower troposphere (Figs. 13h,i).

3) 2200 UTC 26 NOVEMBER 2019

Upper-tropospheric PV anomalies dominated near-surface development directly following the 12-h most rapid deepening period of the NV19 storm (Fig. 11d). Near-surface 1-hourly height changes from the inversion of the UPTROP peaked at 2200 UTC 26 November, which was nearly coincident with the time at which the upper-level jet/front system was most intense (not shown). At this time, the winds associated with UPTROP and INT induced CPVA to the east and south of the NV19 storm, respectively (Figs. 14a,b). There was again no advection of upper-tropospheric PV by the SFC balanced flow near the storm at this time (Fig. 14c). Diabatically induced PV anomalies in the midtroposphere were weaker at this time, with midtropospheric CPVA from each piece of the perturbation flow occurring to the east of the storm center (Figs. 14d–f). Lower-boundary CPVA from the UPTROP and INT balanced flows was situated to the southeast of the NV19 storm center (Figs. 14g,h) with no substantial lower-boundary CPVA arising from the SFC balanced flow (Fig. 14i). Therefore, it appears that mutual cyclonic amplification was primarily occurring in the midtroposphere (Figs. 14d–f) and upper troposphere (Figs. 14a,b) late in the development of the cyclone.

d. Summary

The foregoing analysis reveals that the early propagation of the NV19 DRW was facilitated by column stretching tied to lower-tropospheric frontogenesis along the preexisting baroclinic zone. This frontogenesis was predominantly forced by differential temperature advection associated with the UPTROP balanced flow at 1200 UTC 25 November and then by the SFC balanced flow at 0000 UTC 26 November 2019, at the start of DRW intensification. Analysis of the near-surface height changes suggests that the diabatically induced INT PV was the most prominent contributor to near-surface height changes during the intensification of the NV19 storm. The upper-tropospheric/lower-stratospheric UPTROP PV contributed the most to near-surface height changes during the

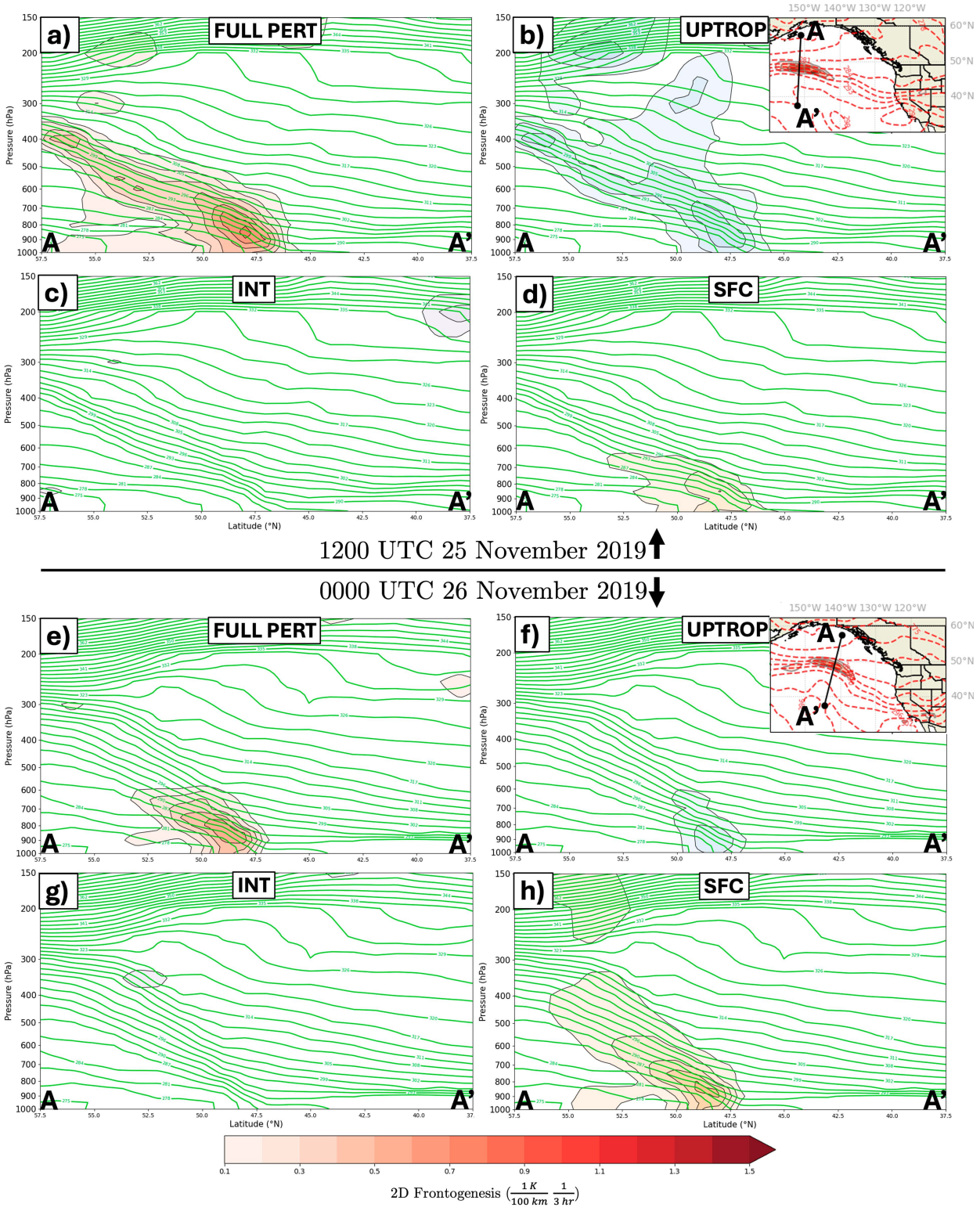

FIG. 10. Frontogenesis associated with discrete portions of the balanced flow derived from piecewise PV inversion. (a) Cross section along A–A′ in Fig. 2c of potential temperature and frontogenesis valid at 1200 UTC 25 Nov 2019. Potential temperature (green) contoured every 3 K starting at 300 K. Positive frontogenesis function from the FULL PERT PV balanced flow (red shading) shaded every 1×10^{-1} K (100 km)$^{-1}$ (3 h)$^{-1}$ and smoothed using a 9-point smoother. (b) Cross section along A–A′ in Fig. 2c of potential temperature

last 12 h of storm intensification just prior to landfall. The lower-tropospheric SFC PV influenced near-surface height changes only very early in the development. Since the SFC PV isolates the effects of lower-boundary θ anomalies, which are influenced by near-surface heat fluxes, the piecewise PV inversion presented here suggests that such fluxes exerted only a marginal influence on the intensification of the NV19 storm.

This suggestion is supported by consideration of ERA5 surface sensible heat data across a $10° \times 10°$ box centered on the NV19 MSLP minimum throughout its evolution. Surface sensible heat flux anomalies are calculated with respect to two different time means: 1) from 1200 UTC 25 November to 0000 UTC 28 November 2019, which captures the entire NV19 storm life cycle, and 2) from 0000 UTC 1 November to 2300 UTC 31 December 2019, the 2-month time mean. Employing the first time mean approach, surface sensible heat flux was anomalously negative throughout the majority of the NV19 storm evolution and was only positive between 0900 UTC 26 November 2019 and 1600 UTC 26 November 2019 (Fig. 15). Using the 2-month time mean, anomalous surface sensible heat flux was negative throughout the entire NV19 life cycle (Fig. 15). Thus, the surface sensible heat flux was anomalously negative for at least a majority, or perhaps all, of the NV19 lifecycle. This marginal influence of both near-surface and surface heat fluxes is a notable difference from previous piecewise PV inversions of DRW explosive cyclogenesis events (Moore et al. 2008; Rivière et al. 2010).

It is also suggested that mutual amplification between discrete pieces of perturbation PV progressed from the lower to the upper troposphere as the NV19 storm experienced a 29-h period of uninterrupted 950-hPa height falls. This progression is visualized in schematic form in Fig. 16 with the colored illustrations representing each piece of the perturbation PV and similarly colored arrows indicating the strength and at which isobaric levels that piece of the perturbation PV contributed to mutual amplification.

Early in the life cycle, only the balanced flow from the INT PV contributed to the amplification of another PV anomaly, namely, the UPTROP PV (Fig. 16a). Therefore, *mutual* amplification was relatively absent. As the storm began its period of rapid intensification, *mutual* amplification became more pervasive as the balanced flow associated with the UPTROP PV amplified the INT PV anomaly, the balanced flow associated with the INT PV amplified both the UPTROP PV and SFC PV anomalies, and the balanced flow associated with the SFC PV served to amplify the INT PV anomaly (Fig. 16b). The mutual amplification signal at this time was strongest from the SFC PV. Toward the end of the rapid deepening period, the balanced flow associated with the SFC PV continued to amplify the INT PV anomaly, but the predominant mutual amplification involved the INT PV and UPTROP PV acting throughout the column (Fig. 16c). At this later time, the mutual amplification signal was strongest in association with the mid- to upper-tropospheric PV anomalies. The strength of the INT PV mutual amplification escalated as the NV19 storm matured and the influence of the UPTROP PV mutual amplification progressively extended throughout the whole depth of the troposphere (Fig. 16). The absence of an initial upper-tropospheric cyclogenetic precursor, coupled with the upward march of dominant developmental processes, suggests that the NV19 storm underwent a bottom-up development like that of Lothar (Wernli et al. 2002). Also, the NV19 storm propagated in the direction of the lower-tropospheric diabatically generated PV anomaly which was located to the east (Figs. 13d–f) and southeast (Figs. 14d–f) of the cyclone center, fitting with the DRW propagation mechanism explained in Tamarin and Kaspi (2016) but with an equatorward rather than a poleward track.

5. Conclusions and discussion

Piecewise PV inversion of an extratropical cyclone in late November 2019 reveals a case of explosive DRW development that was predominantly a function of the influence of diabatic generation of PV associated with latent heat release. Only the late stages of cyclogenesis were dominated by upper-tropospheric and lower-stratospheric PV associated with an upper-level jet/front system. Analysis of the piecewise frontogenesis, the 1-hourly height changes at the location of the 950-hPa vorticity maximum, and mutual cyclonic amplification between perturbation PV anomalies in different layers of the troposphere suggests that the NV19 storm followed a bottom-up development similar to that described by Wernli et al. (2002) in association with Lothar. The current study is, to the authors' knowledge, unique in that it interrogates the nature of an explosive DRW development over a cold ocean surface.

Specific findings from the case study include the following:

1) The development of the NV19 storm was unusual in several ways; the storm track was notably out of phase with other EC events in the northeast Pacific Ocean and the typical DRW propagation direction, the deepening rate ranked higher than the 90th percentile in two separate climatologies, and the maximum deepening location of this storm occurred further east than any other EC event over

←
and frontogenesis valid at 1200 UTC 25 Nov 2019. Potential temperature (green) contoured every 3 K starting at 300 K. Positive frontogenesis function from the UPTROP PV balanced flow (blue shading) shaded every 1×10^{-1} K $(100\ \text{km})^{-1}$ $(3\ \text{h})^{-1}$ and smoothed using a 9-point smoother. (c) As in (b), but for the positive frontogenesis function from the INT PV balanced flow (pink shading). (d) As in (c), but for the positive frontogenesis function from the SFC PV balanced flow (orange shading). (e) As in (a), but for a cross section along A–A′ in Fig. 3c valid at 0000 UTC 26 Nov 2019. (f) As in (b), but for a cross section along A–A′ in Fig. 3c valid at 0000 UTC 26 Nov 2019. (g) As in (c), but for a cross section along A–A′ in Fig. 3c valid at 0000 UTC 26 Nov 2019. (h) As in (d), but for a cross section along A–A′ in Fig. 3c valid at 0000 UTC 26 Nov 2019.

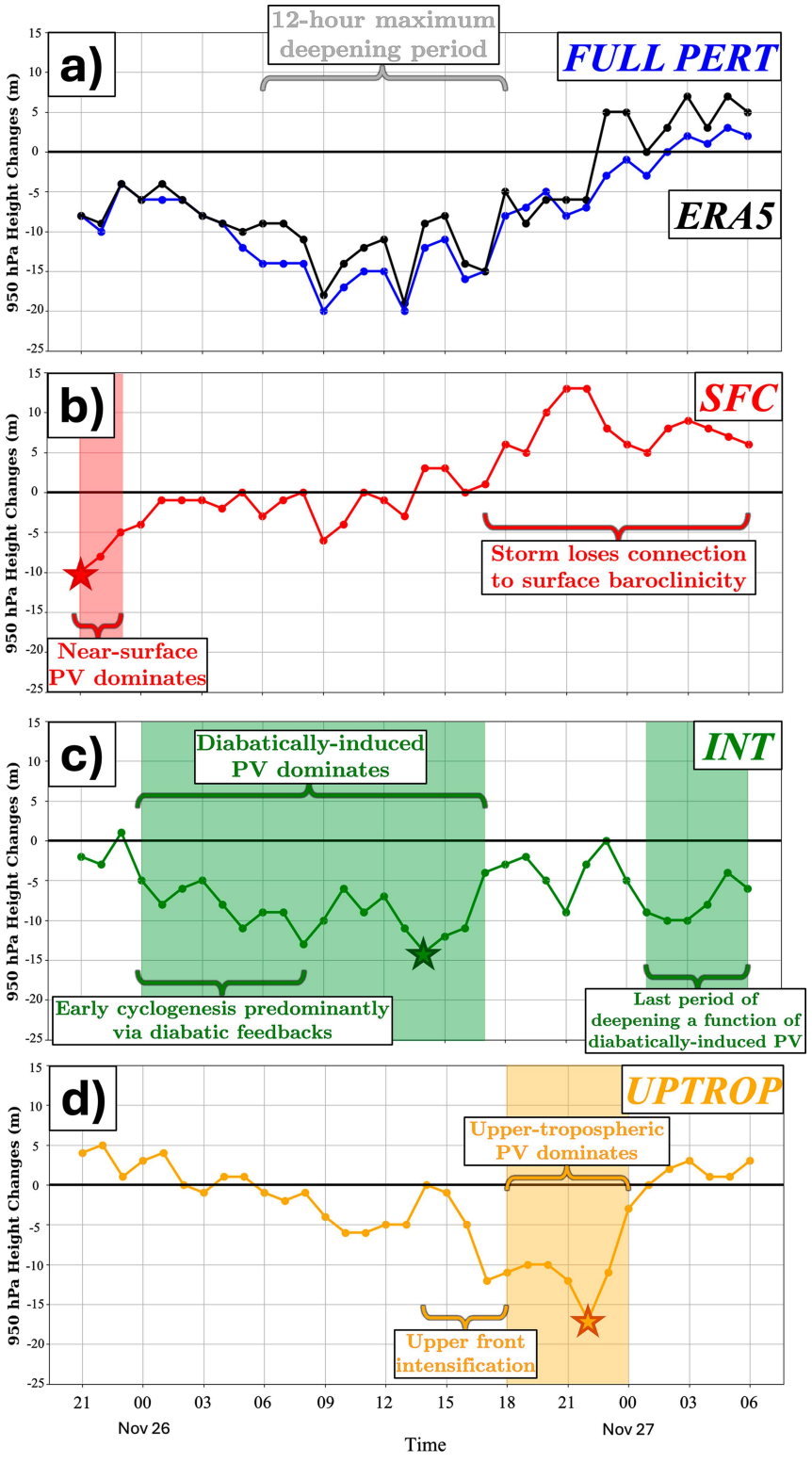

FIG. 11. The 950-hPa 1-hourly height changes from the inversion of the pieces of the perturbation PV at the location of the 950-hPa vorticity maximum of the November 2019 storm. (a) The 950-hPa 1-hourly height changes from the inversion of the FULL PERT PV (blue) as defined in section 3 (see text) along with the observed ERA5 1-hourly height changes (black). Notable time period(s) are annotated. (b) As in (a), but for 1-hourly height changes associated with the SFC PV. Red shading indicates the time period in which the SFC PV contributed the

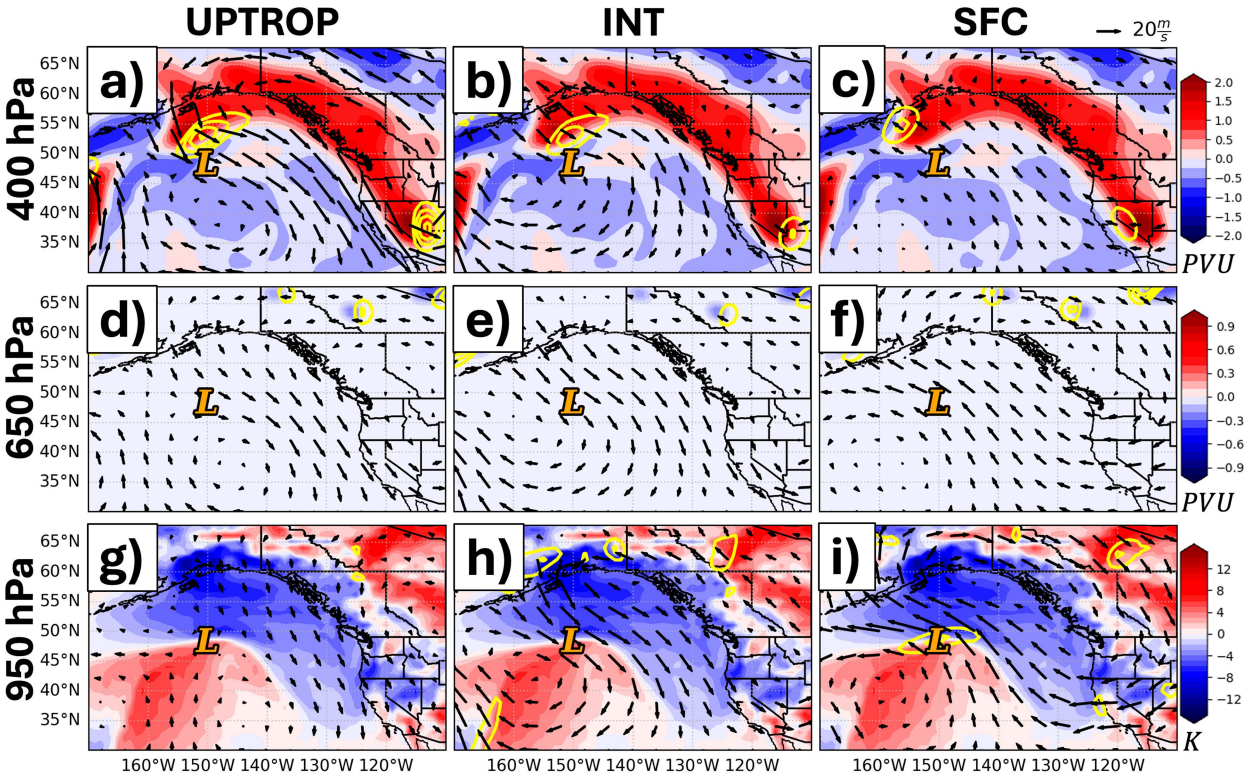

FIG. 12. Balanced flow attributable to the UPTROP, INT, and SFC perturbation PV and the influence of that balanced flow on the 3D PV and potential temperature anomaly structure valid at 2100 UTC 25 Nov 2019. (top) The 400-hPa UPTROP PV anomalies shaded every 0.25 PVU starting at 0.25 PVU and 400-hPa balanced flow (arrows) from the inversion of the (a) UPTROP, (b) INT, and (c) SFC. Yellow, solid contours represent positive UPTROP PV advection by the UPTROP, INT, and SFC balanced flows in (a)–(c), respectively, contoured every 0.1 PVU h^{-1} starting at 0.1 PVU h^{-1}. The location of the 950-hPa relative vorticity maximum is indicated by the orange L. (middle) 650-hPa INT PV anomalies shaded every 0.1 PVU starting at 0.1 PVU and 650-hPa balanced flow (arrows) from the inversion of the (d) UPTROP, (e) INT, and (f) SFC. Yellow, solid contours represent positive INT PV advection by the UPTROP, INT, and SFC balanced flows in (d)–(f), respectively, contoured every starting 0.1 PVU h^{-1} at 0.1 PVU h^{-1}. The location of the 950-hPa relative vorticity maximum is indicated by the orange L. (bottom) The 975-hPa potential temperature anomalies (SFC PV anomalies) shaded every 1 K and the 950-hPa balanced flow from the inversion of the (g) UPTROP, (h) INT, and (i) SFC as represented by the arrows. Yellow, solid contours represent positive surface potential temperature advection by the UPTROP, INT, and SFC balanced flows in (g)–(i), respectively, contoured every 1 K h^{-1} starting at 1 K h^{-1}. The location of the 950-hPa relative vorticity maximum is indicated by the orange L.

the northeast Pacific Ocean in a nonconsecutive 30-yr period.

2) Piecewise frontogenesis analysis, or frontogenesis calculated using the balanced flows from the full column perturbation PV and the three partitioned pieces of the perturbation PV, reveals that frontogenesis along the baroclinic zone stretching across the northeast Pacific Ocean was predominantly a function of balanced winds associated with the UPTROP PV prior to NV19 storm formation and then almost entirely a function of balanced winds associated with the SFC PV as the storm formed and began to strengthen. Thus, the dominant forcing for the lower-tropospheric

←

most negative 950-hPa height changes of all three perturbation PV pieces. The red star indicates the time of the most negative 950-hPa 1-hourly height change from the SFC PV inversion. (c) As in (b), but for 1-hourly height changes associated with the INT PV. Green shading indicates time periods in which the INT PV contributed the most negative 950-hPa height changes of all three perturbation PV pieces. The green star indicates the time of the most negative 950-hPa 1-hourly height change from the INT PV inversion. (d) As in (c), but for 1-hourly height changes associated with the UPTROP PV. Orange shading indicates the time period in which the UPTROP PV contributed the most negative 950-hPa height changes of all three perturbation PV pieces. The orange star indicates the time of the most negative 950-hPa 1-hourly height change from the UPTROP PV inversion.

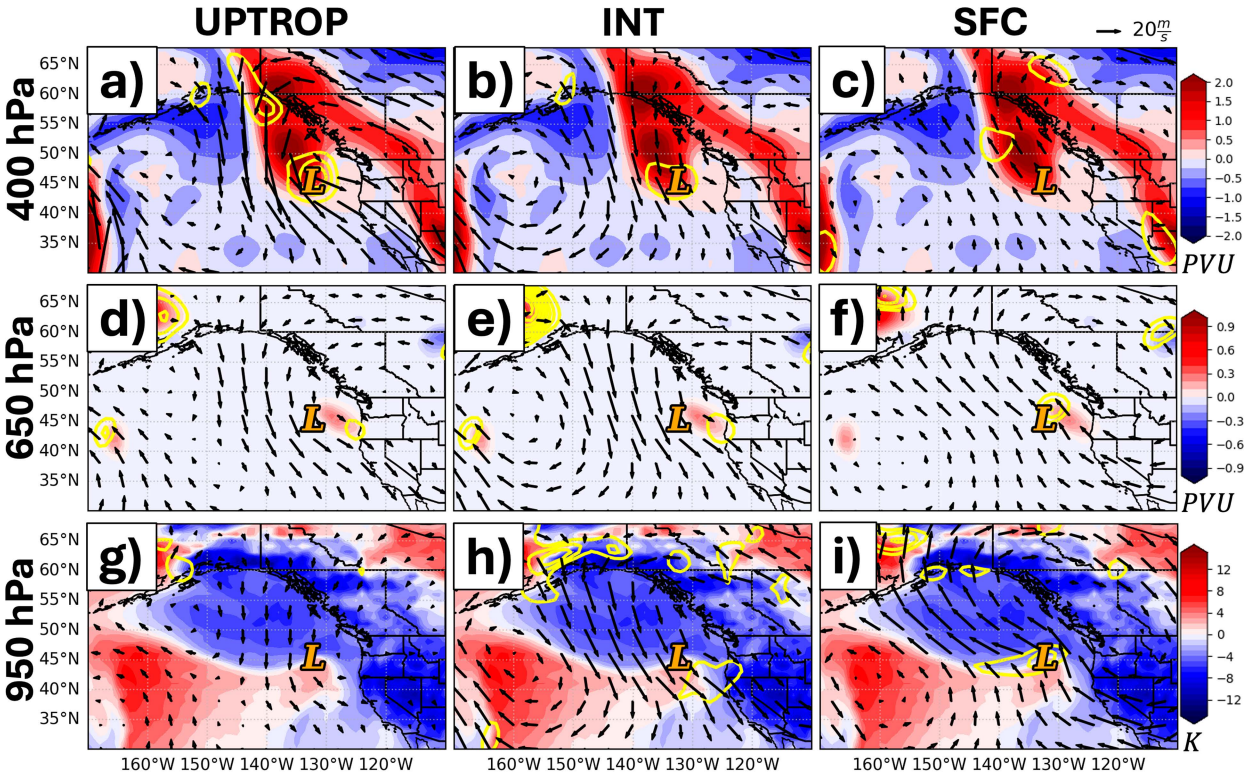

FIG. 13. (a) As in Fig. 12a, but for 1400 UTC 26 Nov 2019. (b) As in Fig. 12b, but for 1400 UTC 26 Nov 2019. (c) As in Fig. 12c, but for 1400 UTC 26 Nov 2019. (d) As in Fig. 12d, but for 1400 UTC 26 Nov 2019. (e) As in Fig. 12e, but for 1400 UTC 26 Nov 2019. (f) As in Fig. 12f, but for 1400 UTC 26 Nov 2019. (g) As in Fig. 12g, but for 1400 UTC 26 Nov 2019. (h) As in Fig. 12h, but for 1400 UTC 26 Nov 2019. (i) As in Fig. 12i, but for 1400 UTC 26 Nov 2019.

frontogenesis that mobilized the DRW was transferred from the upper troposphere prior to initial cyclogenesis to the surface layer once more substantial development had begun.

3) Height falls associated with lower-tropospheric PV dominated in the very early stages of cyclogenesis via the northward transport of high θ (θ_e) air along the cold front of a cutoff cyclone situated to the west of an expansive anticyclone. There was no signal of mutual cyclonic amplification between perturbation PV anomalies throughout the troposphere during this initial formation as the lower-tropospheric DRW formed.
4) Diabatic generation and rearrangement of PV throughout the depth of the troposphere dominated near-surface height falls over the subsequent 16-h period. These diabatic feedbacks were in response to vigorous lower-tropospheric frontogenesis which was situated along the warm front of the NV19 storm. The diabatic feedbacks conspired to force mutual cyclonic amplification of perturbation PV anomalies notably extending throughout the depth of the troposphere. This period encompassed the entire 12-h maximum deepening period during which the storm deepened 34 hPa as it moved southeastward.
5) The final period of development was dominated by upper-tropospheric PV associated with an intense upper-level jet/front system which focused vigorous CVA by the thermal wind directly over the surface cyclone as it approached the coast. Mutual cyclonic amplification was primarily occurring between perturbation PV anomalies in the mid- and upper troposphere during this final period of deepening.
6) The direct effects of near-surface heat fluxes, which are indirectly included in the SFC PV by its definition, were quite unimportant to storm intensification in this case of explosive DRW cyclogenesis. In fact, in contrast to previous piecewise PV inversion studies on rapidly deepening DRWs (Moore et al. 2008; Rivière et al. 2010), the SFC PV was the least important forcing for 950-hPa height falls after the very initial stages of cyclogenesis. This result suggests that explosive DRW developments over a cold ocean rely on either different circumstances or a different sequencing of forcings than explosive DRWs that develop over a warm ocean.

Like Lothar, the NV19 storm featured a bottom-up rapid intensification of a DRW dependent upon the diabatic generation of lower-tropospheric PV to spawn a potent surface cyclone. DRW bottom-up rapid developments resemble the type C cyclogenesis events described in Plant et al. (2003) wherein cyclone intensification is driven by latent heat release, with the addition of strong lower-tropospheric baroclinicity (Boettcher and Wernli 2013; Tamarin and Kaspi 2016).

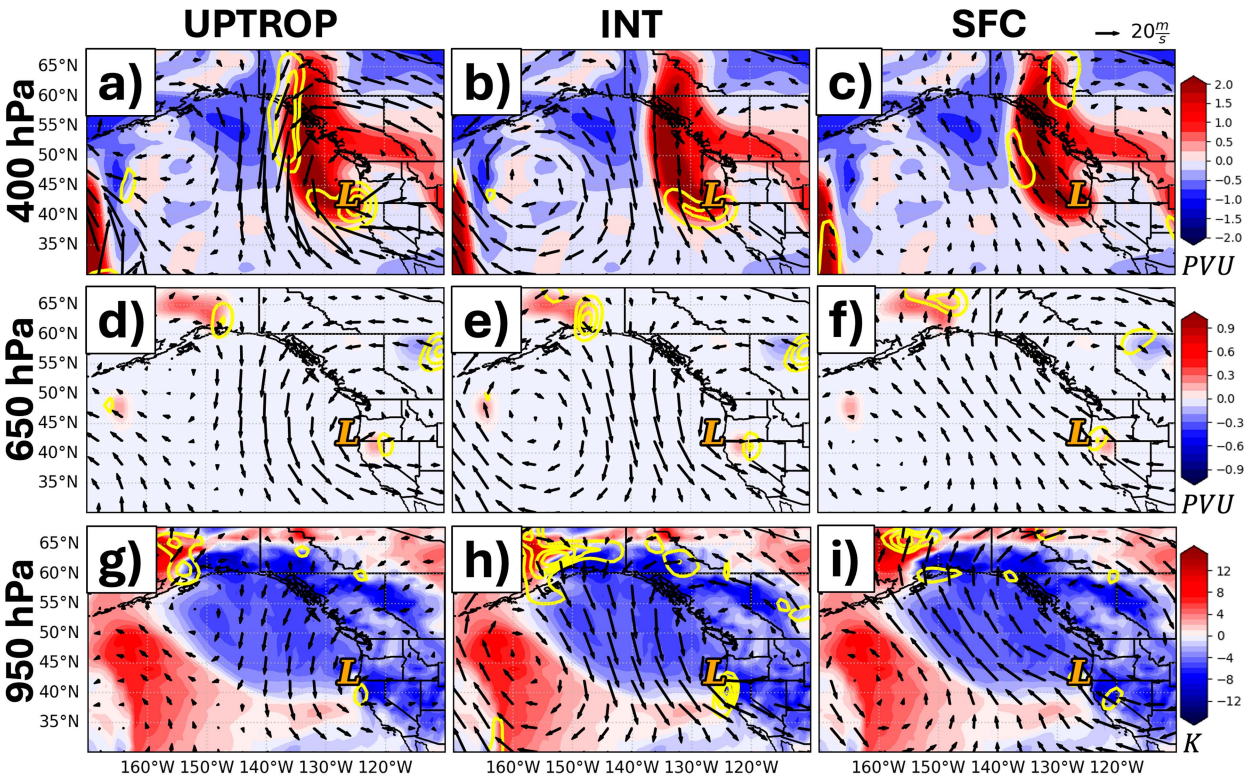

FIG. 14. (a) As in Fig. 13a, but for 2200 UTC 26 Nov 2019. (b) As in Fig. 13b, but for 2200 UTC 26 Nov 2019. (c) As in Fig. 13c, but for 2200 UTC 26 Nov 2019. (d) As in Fig. 13d, but for 2200 UTC 26 Nov 2019. (e) As in Fig. 13e, but for 2200 UTC 26 Nov 2019. (f) As in Fig. 13f, but for 2200 UTC 26 Nov 2019. (g) As in Fig. 13g, but for 2200 UTC 26 Nov 2019. (h) As in Fig. 13h, but for 2200 UTC 26 Nov 2019. (i) As in Fig. 13i, but for 2200 UTC 26 Nov 2019.

Despite several similarities, the NV19 storm did not follow the same developmental sequence as Lothar. Wernli et al. (2002) showed that the circulation attributable to the lower-tropospheric PV anomaly of Lothar, which was produced via intense latent heating, was substantial enough to extend to the jet level and aid in the formation of an upper-tropospheric PV anomaly which then further intensified the low-level PV anomaly through PV superposition (DE; Morgan and Nielsen-Gammon 1998). Though the preceding analysis does not consider the problem directly, it appears that both the lower- and upper-tropospheric PV anomalies associated with the lower-tropospheric DRW vortex and upper-level jet/front system, respectively, initially intensified independently of one another. Additionally, it does not appear that the lower-tropospheric PV anomaly forced the development of the upper-tropospheric PV anomaly, as was the case with Lothar, despite appearing to follow a similar bottom-up development.

Systematic investigation of whether, and to what degree, the simultaneously strengthening lower-tropospheric DRW vortex and upper-level jet/front system had notable influences on one another during the NV19 development is a topic for future work. The specific analysis will focus on whether the circulation associated with the lower-tropospheric DRW vortex contributed to a mobilization of the "Shapiro effect" (Rotunno et al. 1994), thereby instigating the development of the upper-level jet/front system when the two features superposed. This proposition will be explored using piecewise PV inversion in a forthcoming, complementary study on this unusual cyclogenesis event.

Postscript

As the current study neared completion, a DRW over the northeastern Pacific Ocean underwent explosive cyclogenesis from 1200 UTC 18 November 2024 to 0000 UTC 20 November 2024. This event displayed striking dynamical similarities to the event presented in this paper, including a similar structural evolution and very rapid intensification. At 1200 UTC 18 November, the cyclone developed along a zonally oriented baroclinic zone which bisected an anticyclone over the northeast Pacific and was initially driven by lower-tropospheric latent heat release. By 0000 UTC 19 November, an upper-tropospheric shortwave had moved into close proximity to the DRW and focused substantial CVA by the thermal wind (Sutcliffe 1947) over the cyclone center. In the subsequent 24 h, the cyclone deepened an additional 66 hPa, including a 26-hPa pressure fall between 1200 UTC 19 November and 1800 UTC 19 November, matching the maximum 6-h deepening rate accomplished by the Braer storm. The result was an impressive 945-hPa cyclone situated off the Washington, United States, and British Columbia coastline.

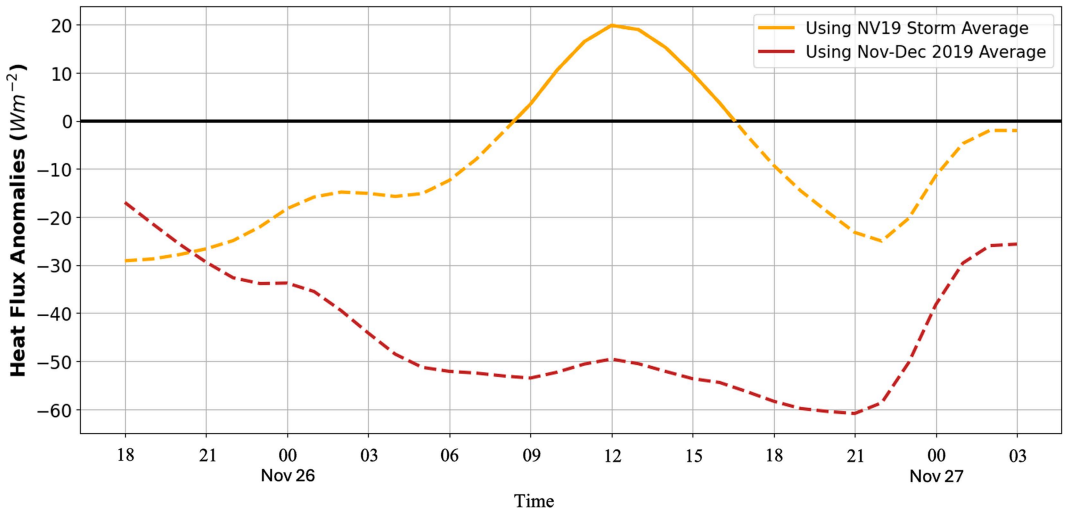

FIG. 15. Surface sensible heat flux anomalies (W m^{-2}) from 1800 UTC 25 Nov 2019 to 0300 UTC 27 Nov 2019 averaged across a 10° × 10° box centered on the NV19 storm. Surface sensible heat flux anomaly relative to the NV19 storm time mean (1200 UTC 25 Nov 2019–0000 UTC 28 Nov 2019) is contoured in solid orange with negative surface sensible heat flux anomaly represented by dashed contours. Surface sensible heat flux anomaly relative to the 2-month time mean (0000 UTC 1 Nov 2019–2300 UTC 31 Dec 2019) is contoured in solid brown with negative surface sensible heat flux anomaly represented by dashed contours.

Both the NV19 storm and this recent event originated as innocuous-looking warm frontal waves, perhaps both as DRWs. Intense and geographically restricted lower-tropospheric frontogenesis produced heavy precipitation which, in turn, generated lower-tropospheric positive PV anomalies along the front. These anomalies orchestrated a period of modest growth before both cyclones were overtaken by potent tropopause-level disturbances which

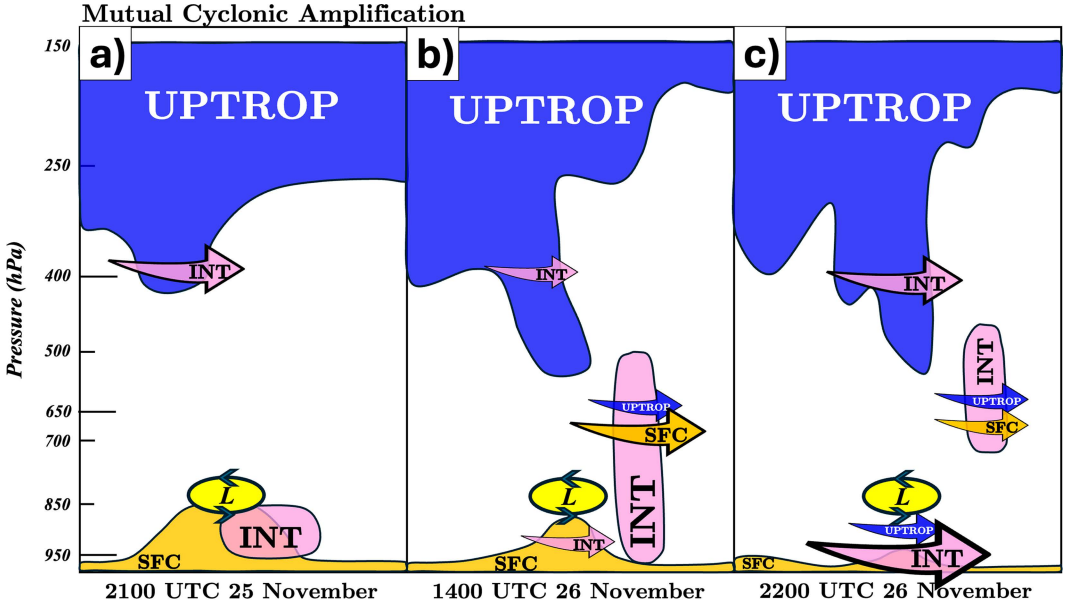

FIG. 16. Schematic of mutual cyclonic amplification during the development of the November 2019 northeast Pacific bomb cyclone. Orange, pink, and blue shapes represent the positive perturbation PV of the SFC, INT, and UPTROP PV, respectively, throughout the troposphere and lower stratosphere (see text for the definition of SFC, INT, and UPTROP). Orange, pink, and blue arrows indicate the perturbation balanced flow of the SFC, INT, and UPTROP PV, respectively, resulting in mutual cyclonic amplification at a specific isobaric level. The size of the arrow indicates the relative strength of mutual cyclonic amplification. The yellow oval and L represent the location of the November 2019 northeast Pacific bomb cyclone center. (a) Mutual cyclonic amplification valid at 2100 UTC 25 Nov 2019. (b) Mutual cyclonic amplification valid at 1400 UTC 26 Nov 2019. (c) Mutual cyclonic amplification valid at 2200 UTC 26 Nov 2019.

facilitated ascent and the stretching of vorticity-rich air that drove the rapid cyclogenesis.

Further investigation of this extraordinary storm is ongoing with the goal of determining the physical importance of the similarities that appear to characterize these two extreme events.

Acknowledgments. The comments of three reviewers and two joint reviewers are appreciated and have greatly improved this manuscript. Chris Davis is acknowledged for developing the piecewise PV inversion code used in the analysis. This paper represents a portion of the first author's dissertation at the University of Wisconsin-Madison. The work was supported by the National Science Foundation under Grant AGS-1851152.

Data availability statement. The fifth generation ECMWF atmospheric reanalysis dataset (ERA5) is produced by the Copernicus Climate Change Service (C3S) at ECMWF and can be accessed via https://cds.climate.copernicus.eu/cdsapp#!/dataset/10.24381/cds.143582cf?tab=overview. Satellite imagery is produced by the National Centers for Environmental Information at NOAA and can be accessed via https://www.ncei.noaa.gov/access. Data used to make in Fig. 7 were adapted from Roebber (1984), Wang and Rogers (2001), and Zhang et al. (2017). All computer programs written to perform the data analysis are available from the authors upon request.

REFERENCES

Ahmadi-Givi, F., G. C. Graig, and R. S. Plant, 2004: The dynamics of a midlatitude cyclone with very strong latent-heat release. *Quart. J. Roy. Meteor. Soc.*, **130**, 295–323, https://doi.org/10.1256/qj.02.226.

Boettcher, M., and H. Wernli, 2011: Life cycle study of a diabatic Rossby wave as a precursor to rapid cyclogenesis in the North Atlantic—Dynamics and forecast performance. *Mon. Wea. Rev.*, **139**, 1861–1878, https://doi.org/10.1175/2011MWR3504.1.

——, and ——, 2013: A 10-yr climatology of diabatic Rossby waves in the Northern Hemisphere. *Mon. Wea. Rev.*, **141**, 1139–1154, https://doi.org/10.1175/MWR-D-12-00012.1.

Bosart, L. F., 1981: The Presidents' Day snowstorm of 18–19 February 1979: A subsynoptic-scale event. *Mon. Wea. Rev.*, **109**, 1542–1566, https://doi.org/10.1175/1520-0493(1981)109<1542:TPDSOF>2.0.CO;2.

Bracegirdle, T. J., and S. L. Gray, 2009: The dynamics of a polar low assessed using potential vorticity inversion. *Quart. J. Roy. Meteor. Soc.*, **135**, 880–893, https://doi.org/10.1002/qj.411.

Bretherton, F. P., 1966: Critical layer instability in baroclinic flows. *Quart. J. Roy. Meteor. Soc.*, **92**, 325–334, https://doi.org/10.1002/qj.49709239302.

Charney, J., 1955: The use of the primitive equations of motion in numerical prediction. *Tellus*, **7A**, 22–26, https://doi.org/10.1111/j.2153-3490.1955.tb01138.x.

Davis, C. A., 1992: Piecewise potential vorticity inversion. *J. Atmos. Sci.*, **49**, 1397–1411, https://doi.org/10.1175/1520-0469(1992)049<1397:PPVI>2.0.CO;2.

——, and K. A. Emanuel, 1988: Observational evidence for the influence of surface heat fluxes on rapid maritime cyclogenesis. *Mon. Wea. Rev.*, **116**, 2649–2659, https://doi.org/10.1175/1520-0493(1988)116<2649:OEFTIO>2.0.CO;2.

——, and ——, 1991: Potential vorticity diagnostics of cyclogenesis. *Mon. Wea. Rev.*, **119**, 1929–1953, https://doi.org/10.1175/1520-0493(1991)119<1929:PVDOC>2.0.CO;2.

——, E. D. Grell, and M. A. Shapiro, 1996: The balanced dynamical nature of a rapidly intensifying oceanic cyclone. *Mon. Wea. Rev.*, **124**, 3–26, https://doi.org/10.1175/1520-0493(1996)124<0003:TBDNOA>2.0.CO;2.

Ertel, H., 1942: Ein neuer hydrodynamischer Erhaltungssatz. *Meteor. Z.*, **59**, 277–282, https://doi.org/10.1007/bf01475602.

Gyakum, J. R., and R. E. Danielson, 2000: Analysis of meteorological precursors to ordinary and explosive cyclogenesis in the western North Pacific. *Mon. Wea. Rev.*, **128**, 851–863, https://doi.org/10.1175/1520-0493(2000)128<0851:AOMPTO>2.0.CO;2.

——, P. J. Roebber, and T. A. Bullock, 1992: The role of antecedent surface vorticity development as a conditioning process in explosive cyclone intensification. *Mon. Wea. Rev.*, **120**, 1465–1489, https://doi.org/10.1175/1520-0493(1992)120<1465:TROASV>2.0.CO;2.

Heo, K.-Y., K.-J. Ha, and T. Ha, 2019: Explosive cyclogenesis around the Korean Peninsula in May 2016 from a potential vorticity perspective: Case study and numerical simulations. *Atmosphere*, **10**, 322, https://doi.org/10.3390/atmos10060322.

Hersbach, H., and Coauthors, 2020: The ERA5 global reanalysis. *Quart. J. Roy. Meteor. Soc.*, **146**, 1999–2049, https://doi.org/10.1002/qj.3803.

Hoskins, B. J., M. E. McIntyre, and A. W. Robertson, 1985: On the use and significance of isentropic potential vorticity maps. *Quart. J. Roy. Meteor. Soc.*, **111**, 877–946, https://doi.org/10.1256/smsqj.47001.

Iizuka, S., M. Shiota, R. Kawamura, and H. Hatsushika, 2013: Influence of the monsoon variability and sea surface temperature front on the explosive cyclone activity in the vicinity of Japan during northern winter. *SOLA*, **9**, 1–4, https://doi.org/10.2151/sola.2013-001.

Iwao, K., M. Inatsu, and M. Kimoto, 2012: Recent changes in explosively developing extratropical cyclones over the winter northwestern Pacific. *J. Climate*, **25**, 7282–7296, https://doi.org/10.1175/JCLI-D-11-00373.1.

Kohl, M., and P. A. O'Gorman, 2022: The diabatic Rossby vortex: Growth rate, length scale, and the wave–vortex transition. *J. Atmos. Sci.*, **79**, 2739–2755, https://doi.org/10.1175/JAS-D-22-0022.1.

Korner, S. O., and J. E. Martin, 2000: Piecewise frontogenesis from a potential vorticity perspective: Methodology and a case study. *Mon. Wea. Rev.*, **128**, 1266–1288, https://doi.org/10.1175/1520-0493(2000)128<1266:PFFAPV>2.0.CO;2.

Kouroutzoglou, J., H. A. Flocas, M. Hatzaki, K. Keay, I. Simmonds, and A. Mavroudis, 2015: On the dynamics of a case study of explosive cyclogenesis in the Mediterranean. *Meteor. Atmos. Phys.*, **127**, 49–73, https://doi.org/10.1007/s00703-014-0357-x.

Kuo, Y.-H., S. Low-Nam, and R. J. Reed, 1991: Effects of surface energy fluxes during the early development and rapid intensification stages of seven explosive cyclones in the Western Atlantic. *Mon. Wea. Rev.*, **119**, 457–476, https://doi.org/10.1175/1520-0493(1991)119<0457:EOSEFD>2.0.CO;2.

Lackmann, G. M., D. Keyser, and L. F. Bosart, 1997: A characteristic life cycle of upper-tropospheric cyclogenetic precursors during the Experiment on Rapidly Intensifying Cyclones over the Atlantic (ERICA). *Mon. Wea. Rev.*, **125**, 2729–2758, https://doi.org/10.1175/1520-0493(1997)125<2729:ACLCOU>2.0.CO;2.

Lagouvardos, K., V. Kotroni, and E. Defer, 2007: The 21–22 January 2004 explosive cyclogenesis over the Aegean Sea: Observations and model analysis. *Quart. J. Roy. Meteor. Soc.*, **133**, 1519–1531, https://doi.org/10.1002/qj.121.

Lang, A. A., and J. E. Martin, 2012: The structure and evolution of lower stratospheric frontal zones. Part 1: Examples in northwesterly and southwesterly flow. *Quart. J. Roy. Meteor. Soc.*, **138**, 1350–1365, https://doi.org/10.1002/qj.843.

Lim, E.-P., and I. Simmonds, 2002: Explosive cyclone development in the Southern Hemisphere and a comparison with Northern Hemisphere events. *Mon. Wea. Rev.*, **130**, 2188–2209, https://doi.org/10.1175/1520-0493(2002)130<2188:ECDITS>2.0.CO;2.

Martin, J. E., 2014: Quasi-geostrophic diagnosis of the influence of vorticity advection on the development of upper level jet-front systems. *Quart. J. Roy. Meteor. Soc.*, **140**, 2658–2671, https://doi.org/10.1002/qj.2333.

——, and J. A. Otkin, 2004: The rapid growth and decay of an extratropical cyclone over the central Pacific Ocean. *Wea. Forecasting*, **19**, 358–376, https://doi.org/10.1175/1520-0434(2004)019<0358:TRGADO>2.0.CO;2.

McKenzie, M. W., 2014: An analysis of numerical weather prediction of the diabatic Rossby Vortex. M.S. thesis, Dept. of Meteorology, Naval Postgraduate School Monterey, 226 pp., https://calhoun.nps.edu/bitstream/handle/10945/42682/14Jun_McKenzie_Matthew.pdf?sequence=1.

Moore, R. W., and M. T. Montgomery, 2004: Reexamining the dynamics of short-scale, diabatic Rossby waves and their role in midlatitude moist cyclogenesis. *J. Atmos. Sci.*, **61**, 754–768, https://doi.org/10.1175/1520-0469(2004)061<0754:RTDOSD>2.0.CO;2.

——, and ——, 2005: Analysis of an idealized, three-dimensional diabatic Rossby vortex: A coherent structure of the moist baroclinic atmosphere. *J. Atmos. Sci.*, **62**, 2703–2725, https://doi.org/10.1175/JAS3472.1.

——, ——, and H. C. Davies, 2008: The integral role of a diabatic Rossby vortex in a heavy snowfall event. *Mon. Wea. Rev.*, **136**, 1878–1897, https://doi.org/10.1175/2007MWR2257.1.

Morgan, M. C., and J. W. Nielsen-Gammon, 1998: Using tropopause maps to diagnose midlatitude weather systems. *Mon. Wea. Rev.*, **126**, 2555–2579, https://doi.org/10.1175/1520-0493(1998)126<2555:UTMTDM>2.0.CO;2.

Odell, L., P. Knippertz, S. Pickering, B. Parkes, and A. Roberts, 2013: The *Braer* storm revisited. *Weather*, **68**, 105–111, https://doi.org/10.1002/wea.2097.

Parker, D. J., and A. J. Thorpe, 1995: Conditional convective heating in a baroclinic atmosphere: A model of convective frontogenesis. *J. Atmos. Sci.*, **52**, 1699–1711, https://doi.org/10.1175/1520-0469(1995)052<1699:CCHIAB>2.0.CO;2.

Plant, R. S., G. C. Craig, and S. L. Gray, 2003: On a threefold classification of extratropical cyclogenesis. *Quart. J. Roy. Meteor. Soc.*, **129**, 2989–3012, https://doi.org/10.1256/qj.02.174.

Raymond, D. J., and H. Jiang, 1990: A theory for long-lived mesoscale convective systems. *J. Atmos. Sci.*, **47**, 3067–3077, https://doi.org/10.1175/1520-0469(1990)047<3067:ATFLLM>2.0.CO;2.

Reed, R. J., and M. D. Albright, 1986: A case study of explosive cyclogenesis in the eastern Pacific. *Mon. Wea. Rev.*, **114**, 2297–2319, https://doi.org/10.1175/1520-0493(1986)114<2297:ACSOEC>2.0.CO;2.

Rivière, G., P. Arbogast, K. Maynard, and A. Joly, 2010: The essential ingredients leading to the explosive growth stage of the European wind storm *Lothar* of Christmas 1999. *Quart. J. Roy. Meteor. Soc.*, **136**, 638–652, https://doi.org/10.1002/qj.585.

Roebber, P. J., 1984: Statistical analysis and updated climatology of explosive cyclones. *Mon. Wea. Rev.*, **112**, 1577–1589, https://doi.org/10.1175/1520-0493(1984)112<1577:SAAUCO>2.0.CO;2.

——, 1989: The role of surface heat and moisture fluxes associated with large-scale ocean current meanders in maritime cyclogenesis. *Mon. Wea. Rev.*, **117**, 1676–1694, https://doi.org/10.1175/1520-0493(1989)117<1676:TROSHA>2.0.CO;2.

——, 1993: A diagnostic case study of self-development as an antecedent conditioning process in explosive cyclogenesis. *Mon. Wea. Rev.*, **121**, 976–1006, https://doi.org/10.1175/1520-0493(1993)121<0976:ADCSOS>2.0.CO;2.

Rossby, C.-G., 1940: Planetary flow patterns in the atmosphere. *Quart. J. Roy. Meteor. Soc.*, **66**, 68–87, https://doi.org/10.1002/j.1477-870X.1940.tb00130.x.

Rotunno, R., W. C. Skamarock, and C. Snyder, 1994: An analysis of frontogenesis in numerical simulations of baroclinic waves. *J. Atmos. Sci.*, **51**, 3373–3398, https://doi.org/10.1175/1520-0469(1994)051<3373:AAOFIN>2.0.CO;2.

Sanders, F., 1986: Explosive cyclogenesis in the west-central North Atlantic Ocean, 1981–84. Part I: Composite structure and mean behavior. *Mon. Wea. Rev.*, **114**, 1781–1794, https://doi.org/10.1175/1520-0493(1986)114<1781:ECITWC>2.0.CO;2.

——, and J. R. Gyakum, 1980: Synoptic-dynamic climatology of the "bomb". *Mon. Wea. Rev.*, **108**, 1589–1606, https://doi.org/10.1175/1520-0493(1980)108<1589:SDCOT>2.0.CO;2.

Shapiro, M. A., 1981: Frontogenesis and geostrophically forced secondary circulations in the vicinity of jet stream-frontal zone systems. *J. Atmos. Sci.*, **38**, 954–973, https://doi.org/10.1175/1520-0469(1981)038<0954:FAGFSC>2.0.CO;2.

——, 1983: Mesoscale weather systems of the central United States. CIRES Tech. Rep., 128 pp., https://repository.library.noaa.gov/view/noaa/48868/noaa_48868_DS1.pdf.

Snyder, C., and R. S. Lindzen, 1991: Quasi-geostrophic wave-CISK in an unbounded baroclinic shear. *J. Atmos. Sci.*, **48**, 76–86, https://doi.org/10.1175/1520-0469(1991)048<0076:QGWCIA>2.0.CO;2.

Sutcliffe, R. C., 1947: A contribution to the problem of development. *Quart. J. Roy. Meteor. Soc.*, **73**, 370–383, https://doi.org/10.1002/qj.49707331710.

Tamarin, T., and Y. Kaspi, 2016: The poleward motion of extratropical cyclones from a potential vorticity tendency analysis. *J. Atmos. Sci.*, **73**, 1687–1707, https://doi.org/10.1175/JAS-D-15-0168.1.

Terpstra, A., T. Spengler, and R. W. Moore, 2015: Idealised simulations of polar low development in an Arctic moist-baroclinic environment. *Quart. J. Roy. Meteor. Soc.*, **141**, 1987–1996, https://doi.org/10.1002/qj.2507.

Wang, C.-C., and J. C. Rogers, 2001: A composite study of explosive cyclogenesis in different sectors of the North Atlantic. Part I: Cyclone structure and evolution. *Mon. Wea. Rev.*, **129**, 1481–1499, https://doi.org/10.1175/1520-0493(2001)129<1481:ACSOEC>2.0.CO;2.

Weldon, R. B., 1979: Cloud patterns and the upper air wind field. Air Weather Service Tech. Rep. AWS/TR-79/003, 104 pp., https://apps.dtic.mil/sti/tr/pdf/ADA099155.pdf.

Wernli, H., S. Dirren, M. A. Liniger, and M. Zillig, 2002: Dynamical aspects of the life cycle of the winter storm 'Lothar' (24–26 December 1999). *Quart. J. Roy. Meteor. Soc.*, **128**, 405–429, https://doi.org/10.1256/003590002321042036.

Winters, A. C., and J. E. Martin, 2017: Diagnosis of a North American polar–subtropical jet superposition employing

piecewise potential vorticity inversion. *Mon. Wea. Rev.*, **145**, 1853–1873, https://doi.org/10.1175/MWR-D-16-0262.1.

Yoshiike, S., and R. Kawamura, 2009: Influence of wintertime large-scale circulation on the explosively developing cyclones over the western North Pacific and their downstream effects. *J. Geophys. Res.*, **114**, D13110, https://doi.org/10.1029/2009JD011820.

Zhang, G., and Z. Wang, 2018: North Atlantic extratropical Rossby wave breaking during the warm season: Wave life cycle and role of diabatic heating. *Mon. Wea. Rev.*, **146**, 695–712, https://doi.org/10.1175/MWR-D-17-0204.1.

Zhang, S., G. Fu, C. Lu, and J. Liu, 2017: Characteristics of explosive cyclones over the northern Pacific. *J. Appl. Meteor. Climatol.*, **56**, 3187–3210, https://doi.org/10.1175/JAMC-D-16-0330.1.